Received: 6 December 2021 | Revised: 2 June 2022 | Accepted: 4 June 2022

DOI: 10.1111/jnc.15653

Journal of Neurochemistry JNC The Official Journal of the International Society for Neurochemistry WILEY

ORIGINAL ARTICLE

3D imaging of supraspinal inputs to the thoracic and lumbar spinal cord mapped by retrograde tracing and light-sheet microscopy

Tao Lu[1] | Munehisa Shinozaki[1] | Narihito Nagoshi[2] | Masaya Nakamura[2] | Hideyuki Okano[1]

[1]Department of Physiology, Keio University School of Medicine, Tokyo, Japan

[2]Department of Orthopaedic Surgery, Keio University School of Medicine, Tokyo, Japan

Correspondence
Masaya Nakamura, Department of Orthopaedic Surgery, Keio University School of Medicine, 35 Shinanomachi, Shinjuku-ku, Tokyo 160-8582, Japan.
Email: masa@keio.jp

Hideyuki Okano, Department of Physiology, Keio University School of Medicine, 35 Shinanomachi, Shinjuku-ku, Tokyo 160-8582, Japan.
Email: hidokano@keio.jp

Funding information
Japan Agency for Medical Research and Development, Grant/Award Number: JP20bm0204001, JP19bm0204001 and JP18bk0104017; Japan Science and Technology Agency, Grant/Award Number: JPMJSP2123

Cover Image for this issue: https://doi.org/10.1111/jnc.15414

Abstract

The supraspinal inputs play a major role in tuning the hindlimb locomotion function. While most research on spinal cord injury (SCI) with rodents is based on thoracic segments, the difference in connectivity of the supraspinal centers to the thoracic and lumbar cord is still unknown. Here, we combined retrograde tracing and 3D imaging to map the connectivity of supraspinal neurons projecting to thoracic (T9-vertebral) and lumbar (T13-vertebral) spinal levels in adult female mice. We dissected the difference in connections of corticospinal neurons (CSNs), rubrospinal neurons, and reticulospinal neurons projecting to thoracic and lumbar cords. The ratio of double-labeled neurons is higher in T13-vertebral projection CSNs and parvocellular part of the red nucleus (RPC) than in T9-vertebral projection. Using the Cre-DIO system, we precisely targeted CSNs projecting to T9-vertebral or T13-vertebral. We found that abundant axon branches communicated with the red nucleus and reticular formation and distributed from cervical gray matter to the lumbar cord. Their collateral branches showed a distinct innervation pattern in thoracic and lumbar gray matters and a similar distribution pattern in the cervical spinal cord. These results revealed the difference in connectivity between the thoracic and lumbar projection supraspinal centers and clarified the collateralization of thoracic/lumbar projection CSNs throughout the brain and spinal cord. This study highlights brain-spinal cord neural networks and the complexity of the axon terminals of spinal projection CSNs, which could contribute to the development of targeted therapeutic strategies connecting CST fibers and hindlimb function recovery.

KEYWORDS
collateral branches, innervation pattern, light-sheet microscopy, retrograde tracing, supraspinal inputs, tissue clearing

Abbreviations: AAV, adeno-associated virus; ANOVA, analysis of variance; BABB, a mixture of benzyl alcohol and benzyl benzoate; BDA, biotinylated dextran amine; CFA, caudal forelimb area; CSNs, corticospinal neurons; CST, corticospinal tract; CTB, Cholera Toxin Subunit B; DF, degrees of freedom; DRGs, dorsal root ganglia neurons; EGFP, enhanced green fluorescent protein; hiPSC-NS/PCs, human induced pluripotent stem cell-derived neural stem/progenitor cells; LOTUS-Tg, LOTUS-over-expressing; RFA, rostral forelimb area; RMC, magnocellular part of the red nucleus; RST, rubrospinal tract; RtST, reticulospinal tract; RSNs, rubrospinal neurons; RtSNs, reticulospinal neurons; RPC, parvocellular region of the red nucleus; SCI, spinal cord injury; THF, tetrahydrofuran.

1 | INTRODUCTION

Approximately 0.93 million people worldwide suffer from spinal cord injury (SCI) with severe sequelae each year, justifying the intense research on treatments for SCI (Asboth et al., 2018; Shinozaki et al., 2021). The descending pathway originates from various brain nuclei and finally converges into specific areas in the spinal cord (Lemon, 2008; Liang et al., 2011). Supraspinal inputs are necessary movement commands that regulate normal activities mediated by the corresponding descending tracts, including the corticospinal tract (CST), the rubrospinal tract (RST), and the reticulospinal tract (RtST) (Engmann et al., 2020; Wang et al., 2017; Williams & Martin, 2015). Thoracic spinal cord injury (SCI) models have been commonly used to study function recovery after stem cell transplantation (Lu et al., 2020). Our previous studies have achieved recovery of hindlimb function in the subacute phase of 10th thoracic (T10) SCI models using human induced pluripotent stem cell-derived neural stem/progenitor cells (hiPSC-NS/PCs) therapy (Kajikawa et al., 2020; Kojima et al., 2019; Okubo et al., 2018; Tsuji et al., 2010). One mechanism of stem cell therapy for SCI is neuronal relays, which rewire supraspinal inputs (rostral) and spared local circuits remaining below the lesion (caudal) (Shinozaki et al., 2021). However, the difference in connectivity of the supraspinal neurons that project to the thoracic and lumbar cords is still unrevealed. The essential spinal regions are located in the rostral and caudal positions of the lesion in the SCI model, where the cells are often experimentally implanted to form a relay circuit.

Efficient retrograde tracing for long-range connections formed by projection neurons constitutes a mandatory requirement for neural circuit dissection (Sheikh et al., 2018). In consideration of retrograde labeling efficiency, a newly developed retrograde serotype, AAV2-Retro, is a useful tool to illustrate supraspinal neurons projecting to the injection site (Tervo et al., 2016). Cervical- and lumbar-projection supraspinal neurons have been reported in several studies (Kamiyama et al., 2015; Steward et al., 2021; Wang et al., 2018). A misgiving from these studies is that a fraction of corticospinal neurons (CSNs) co-expressed different fluorescence after cervical and lumbar injection. An interpretation is that these neurons innervate in both the cervical and lumbar segment (Kamiyama et al., 2015). However, evidence for multiple spinal segments innervation of double-labeled neurons is still unclear. Previous studies have reported some CST collaterals in the striatum, reticular formation, and cervical spinal cord (Kita & Kita, 2012; Network, 2021; Wang et al., 2017). Besides, BDA anterograde tracing studies in multiple cortex areas also revealed that those CST axons innervated in different spinal segments (Steward et al., 2021). However, no studies report the axon collateral network of single thoracic/lumbar segment projection CSNs.

To know the supraspinal connections to the thoracic and lumbar cords, T9-vertebral and T13-vertebral level injections of AAV2-Retro-mCherry/EGFP were performed separately. First, we demonstrated that AAV2-Retro rapidly transduced supraspinal neurons after lumbar injection, including CSNs, rubrospinal neurons (RSNs), and reticulospinal neurons (RtSNs). Using layer V marker (Ctip2) and BDA anterograde tracing, we confirmed the correct labeling capacity of AAV2-Retro for CSNs and CST axons. Then, quantitation analysis revealed a distinct anatomical position of these neurons in adult female mice: (1) the T9-vertebral projection CSNs reside in a broader cortical area than T13-vertebral projection, distributed medially and laterally; (2) in the caudal portion of the red nucleus, T9-vertebral and T13-vertebral projection magnocellular (RMC) population were separated into two distinct groups with some double-labeled neurons, meanwhile, in rostral area of red nucleus, T9-vertebral projection parvocellular (RPC) population shows higher numbers than the T13-vertebral projection; (3) a similar distribution pattern of T9-vertebral and T13-vertebral projection RtSNs. Notably, a higher ratio of double-labeled neurons was observed in CSNs and RPC neurons projecting to T13-vertebral. Next, tissue clearing and light-sheet microscopy illustrated the spatial relationship of these neurons and tracts. Finally, we selectively targeted the CSNs projecting to T9-vertebral or T13-vertebral using the Cre-DIO system. Interestingly, we found that the axon branches of those neurons innervated in other regions of the brain and multiple spinal segments, which have a distinct innervation pattern in thoracic and lumbar gray matters, and similar distribution patterns in the cervical spinal cord. Overall, these results reveal the difference in connectivity of supraspinal inputs to the thoracic and lumbar segments and provide new insights into the collateralization of single thoracic/lumbar segment projection CSNs.

2 | MATERIALS AND METHODS

2.1 | Animals

All animal experiments were approved by the Ethics Committee of Keio University (approval number: 19022) and were carefully conducted following the Guide for the Care and Use of Laboratory Animals (NIH, USA). Wild-type C57BL/6J adult mice (female, 8w, 18–22 g, RRID: IMSR_JAX:000664) were used in this study. Animals were purchased from CLEA CO., LTD (Tokyo, Japan). Animals were housed in a temperature-controlled environment (with a constant 12 h light/dark cycle), with access to food and water ad libitum throughout this study. No randomization was performed to allocate animals in this study. Animals were arbitrarily placed in cages (1–5 animals/cage). The study was not pre-registered. Experiments on animals were started under anesthesia to minimize animal suffering when no foot pain reaction was evoked by forceps. After surgery and injection, the mice were kept on a thermostatically controlled heating pad (38°C) until fully recovered. Ketamine has a strong analgesic effect (Slingsby & Waterman-Pearson, 2000; Wagner et al., 2002), and no animal showed signs of allodynia defined by the animal committee.

2.2 | Virus production and injection

AAV2-Retro-hSyn-EGFP (cat.no. 50465; titer ≥7×10^{12} vg/ml), AAV2-Retro-hSyn-mCherry (cat.no. 114472; titer ≥7×10^{12} vg/ml),

AAV2-hSyn-DIO-EGFP (cat.no. 50457-AAV2; titer ≥3×10^{12} vg/ml) and AAV2-Retro-pgk-Cre (cat.no. 24593-AAVrg; titer ≥7×10^{12} vg/ml) were purchased from Addgene (RRID:SCR_002037). As recommended by the Institutional Guidelines on Animal Experimentation at Keio University (approval number: 19022), all mice were anesthetized with ketamine (60 mg/kg) and xylazine (10 mg/kg) by intraperitoneal (ip) injection. The laminal plates of the thirteenth thoracic (T13-vertebral, equal to L4 spinal segment) and ninth thoracic (T9-vertebral, equal to T12 spinal segment) vertebrae were removed (Harrison et al., 2013). Viruses were unilaterally injected into the spinal cord using pulled glass micropipettes driven by an air pressure pump (BJ110, BEX, Japan) for 7 min, and the needle was held in place for 5 min before being slowly retracted for 5 min (Peters et al., 2017). 0.4 μl AAV virus was unilaterally injected into T9, 0.4 mm lateral to the midline at a depth of 0.6 mm. For lumbar injection (T13), the spinous process T12 was used as a landmark. Then, 0.5 μl AAV virus was unilaterally injected as described above, 0.5 mm lateral to the midline at a depth of 0.7 mm. In the tissue clearing and 3D reconstruction group, the virus was bilaterally injected into corresponding spinal cords using the method described above.

For intersectional targeting of CSNs projecting to T9-vertebral or T13-vertebral (Kinoshita et al., 2012; Liu et al., 2017), all injections are similar to the procedures mentioned above. Injection coordinates were used as previously described with slightly modified (Ito et al., 2018). Briefly, AAV2-hSyn-DIO-EGFP (150 nl/site) was injected bilaterally into the motor cortex at four locations: 0.8- and 1.5-mm lateral to the midline and 0.5- and 1.5-mm posterior from the bregma at a depth of 0.7 mm. Then, AAV2-Retro-pgk-Cre (200 nL/site) was injected bilaterally into the spinal cord at T9-vertebral or T13-vertebral level.

2.3 | Tissue processing and imaging

Animals were anesthetized with ketamine (60 mg/kg) and xylazine (10 mg/kg) by intraperitoneal (ip) injection. Then, mice were transcardially perfused with saline and 4% paraformaldehyde solution. Brains and spinal cords were dissected and fixed overnight in 4% paraformaldehyde at 4°C. After fixation, brains were stored separately at 0.05%NaN_3/PBS solutions. The spinal cords were immersed in 10% sucrose overnight at 4°C, followed by 30% sucrose, then embedded in OCT compound (Sakura, Japan) before sectioning. Samples were cut into 20-μm axial sections using a cryostat. Brains were first separated into three parts using Rodent Brain Matrix (ASI-Instruments) according to the anatomical positions of the sensorimotor cortex, red nuclei, and reticular formation. A complete series of 60-μm brain coronal sections were collected using a vibratome (VT1200s, Leica). Brain sections were mounted on slides and imaged with a confocal and a Keyence epifluorescence microscope. The fluorescent signals of EGFP and mCherry were strong enough to image without antibody amplification. According to the Allen Brain Atlas, the anatomical locations of fluorescent structures were calibrated according to the nomenclature of anatomical structures (Wang et al., 2018).

2.4 | Immunohistochemistry

Tissue sections were stained with the following primary antibodies overnight at 4°C: anti-Cre (rabbit, IgG, Biolegend, cat.no.908001, 1:250, RRID:AB_2565079), anti-Ctip2 (rat, IgG2a, Abcam, cat.no. Ab18465, 1:500, RRID:AB_2064130), anti-Foxp2 (goat, IgG, Abcam, cat.no. Ab1307, 1:500, RRID:AB_1268914), anti-GAD67 (mouse, IgG2a, Sigma-Aldrich, cat.no. MAB5406, 1:200, RRID:AB_2278725), anti-GFP (chicken IgY, Aves Labs, cat.no. GFP-1020, 1:1000, RRID:AB_10000240), anti-Glutamate receptor 2/3 (rabbit, IgG, Sigma-Aldrich, cat.no.AGT-012, 1:100, RRID:AB_90710), anti-GlyT2 (rabbit, IgG, allomone labs, cat.no.AB1506, 1:50, RRID:AB_11121049), anti-5-HT (rabbit, IgG, ImmunoStar, cat. no.20080, 1:200, RRID:AB_572263), anti-HuC/D (mouse, IgG2b, Invitrogen, cat.no. A-21271, 1:100, RRID:AB_221448), anti-mCherry (rabbit, IgG, Abcam, cat.no. Ab167453, 1:500, RRID:AB_2571870), anti-NeuN (mouse, IgG1, Chemicon, cat.no. MAB377, 1:500, RRID:AB_2298767), anti-pan-ELAVL (Hu) (human IgG, 1:1000; a gift from Dr. Robert Darnell, Rockefeller University, USA), anti-vGAT (mouse, IgG3, Synaptic system, cat.no.131011, 1:100, RRID:AB_887872), and anti-vGLUT1 (rabbit, IgG, Synaptic system, cat. no. 135303, 1:400, RRID:AB_887875). Sections were then incubated for 2 h (brain sections) or 1 h (spinal sections) at room temperature (25°C) with anti-mouse, anti-goat, anti-chicken, anti-rat, anti-human, and anti-rabbit Alexa Fluor-conjugated secondary antibodies (1:1000; Invitrogen Life Technologies, RRID:AB_142924, RRID:AB_141844, RRID:AB_141733, RRID:AB_141596, RRID:AB_1500627, RRID:AB_1500897, RRID:AB_2535813) and Hoechst 33258 (10 μg/ml, Sigma-Aldrich). All images were captured using Keyence microscope (BZ-X710, Japan) and confocal microscope (LSM700, Zeiss, Germany).

2.5 | Anterograde labeling of the CST

Two weeks after injection of AAV2-Retro-EGFP, mice were anesthetized with ketamine (60 mg/kg) and xylazine (10 mg/kg) by intraperitoneal (ip) injection, then mounted on a stereotaxic instrument (NARISHIGE Group, Tokyo, Japan). A square area of the skull with a 1 mm diameter was carefully removed using a micro-driller (Model: CMD-1000, Muromachi Kikai CO., LTD, Tokyo, Japan) to expose the left cortical sensorimotor area. The biotinylated dextran amine (10% 10 k BDA/DW, Invitrogen) solutions (0.3 μl/site) were slowly injected into the left sensorimotor cortex at 4 locations to trace CST fibers ($n = 4$) at the following coordinates: 0.5- and 1.5-mm lateral to the midline, 0.5- and 1.5-mm posterior from the bregma at a depth of 0.7 mm (Ito et al., 2018). 2w after injection, the mice were sacrificed using the same perfusion method mentioned above. 20-μm axial thoracic spinal sections were cut using a cryostat. BDA was visualized using Alexa Fluor 555 conjugated streptavidin, and images were captured using a Keyence and LSM700 microscope.

2.6 | Quantitative analysis

2.6.1 | Quantification of supraspinal neurons

To measure the number of EGFP$^+$ neurons, a series of 60 μm brain coronal sections (every-third section, in 120-μm gaps) collected across the entire positive area in the sensorimotor cortex, red nucleus, and reticular formation were used and captured using a 20x objective (LSM700, Zeiss). These images were imported into Fiji (NIH, USA). The total numbers of EGFP$^+$ neurons co-localized with the Hoechst signal in the sensorimotor cortex, red nucleus, and reticular formation were manually used and counted by individuals who were blinded to the groups.

To measure the anatomical position of T9-vertebral and T13-vertebral level projection CSNs (n = 4), RSNs, and RtSNs (n = 6.6), a series of 60 μm brain coronal sections (every-fourth section, in 180-μm gaps) collected across the entire positive area in the sensorimotor cortex, red nucleus, and reticular formation were used and captured using a 20x objective (LSM700, Zeiss). The sensorimotor cortex was separated into three parts from medial to lateral, <1000 μm, 1000–1500 μm, and 1500–2200 μm. Cell bodies were blindly counted using a plugin in Fiji (Point picker, NIH, USA) as previously described (Ueno et al., 2018).

To identify the precise distribution of T9-vertebral (mCherry$^+$) and T13-vertebral (EGFP$^+$) projection CSNs, a complete series of 60-μm brain coronal sections (about 42 sections per animal; n = 3) were imaged, ranging from the first visible fluorescent cell bodies to the last ones. The midline must also be captured as a counting landmark. The cortex was then separated at 100 μm from the midline to the lateral side using Zen software (Zeiss, Germany). Then, those EGFP$^+$ and/or mCherry$^+$ neurons (Soma size: 19.7 ± 0.6 μm) in each panel per 6000 μm^2 (60 μm thickness × 100 μm interval = 6000 μm^2) were blindly counted as described above. Subsequently, a visualization heatmap for these data was generated using the TBtools toolkit (Chen et al., 2020; Oswald et al., 2013).

2.6.2 | Quantification of EGFP expression

To evaluate the time course of EGFP expression after injection into the lumbar spinal cord, the dorsal funiculus of cervical enlargement sections was captured with the same exposure settings at ×40 magnification on a confocal microscope (LSM700). Analysis and quantification were calculated in Fiji (NIH). GFP antibody was used to reduce bias during tissue processing. At least three sections of the same cervical enlargement per animal were examined (Wang et al., 2017).

2.6.3 | Quantification of CST axon density in spinal gray matter

The branches of the CST axon in the spinal gray matter of cervical enlargement, middle thoracic, and lumbar enlargement were divided into three areas: dorsal (lamina I–IV), medial (lamina V–VI), and ventral (VII–X) parts. The percentages of axon density (EGFP$^+$) in each area were quantified with Fiji (NIH) using three confocal image stacks per animal (Gu et al., 2019).

2.6.4 | Distribution of axon collaterals in the spinal gray matters

The images were acquired from upper cervical, cervical enlargement, cervical-thoracic, caudal thoracic, thoracic-lumbar, and lumbar enlargement using a Keyence microscope. The heatmaps were generated using a Processing programming language. Seven to nine axial spinal sections were analyzed for each animal.

2.7 | Tissue clearing and light-sheet imaging

Whole brains and spinal cords were removed and fixed in 4% paraformaldehyde at 4°C overnight and rinsed three times in 0.1 M PBS (pH 7.4), then stored in 0.05%NaN_3/PBS. The dura was carefully and completely removed using forceps before the clearing process. Tissue clearing using modified 3DISCO was performed as previously described (Soderblom et al., 2015). The samples were incubated on a rotating wheel at room temperature (25°C) in 50, 80, and 100% tetrahydrofuran (THF; Sigma-Aldrich, 401 757; 2019), each for 1 h for spinal tissue, 10 h for brains, and then immersed in 100% THF overnight. After THF treatment, samples were transferred to BABB solution (mixture of benzyl alcohol, sigma, 305 197, 2020; and benzyl benzoate, Nacalai, 04601–65, 2020 in a 1:2 ratio) for 1–3 h. After clearing, samples were immediately imaged using a Z1 light-sheet microscope (Z.1, Zeiss) equipped with a 5× Plan Neofluar objective. Image analysis and 3D reconstructions were performed using Zen software and 3Dscript (Schmid et al., 2019), a plugin in Fiji software. After removing the autofluorescence using the Background Subtraction function, movies were generated using programming languages in 3Dscript and merged in Photoshop CS6 (Adobe Systems Inc.).

2.8 | Experimental design and statistical analysis

In total, 61 mice were used. Six mice were excluded because of mistargeted injection. For testing retrograde transduction capacity and time-course experiments, mice were sacrificed at 1w, 2w, 3w, and 4w after injection (n = 8, 9, 10, 9). One mouse in the 2w group and 4w group, and two mice in the 3w group were excluded because of mistargeted injection (failure labeling or transduced bilaterally). In the double tracing experiment (T9-vertebral and T13-vertebral projection), mice were sacrificed 4w after injection (n = 8). Two mice were excluded because of mistargeted injection (failure labeling or transduced bilaterally). Three mice in the double tracing experiment were used in the heatmap of CSNs (T9-vertebral and T13-vertebral projection) (n = 3). BDA anterograde tracing for CST was performed 2w after AAV2-Retro-EGFP

injection ($n = 4$). Mice used for the intersectional strategy to target spinal projection CSNs (T9-vertebral or T13-vertebral level) were sacrificed at 4w after injection ($n = 3, 3$). In tissue clearing and 3D reconstruction experiments, other mice were used ($n = 3$ for double labeling of supraspinal neurons projecting to T9-vertebral and T13-vertebral levels; $n = 2, 2$ for CSNs projecting to T9-vertebral or T13-vertebral level). All data were presented as mean ± SEM and analyzed using Fiji and GraphPad Prism 8.0 (GraphPad Inc. RRID: SCR_002798). No sample calculation was performed. The number of animals used was determined based on previous studies (Kamiyama et al., 2015; Wang et al., 2018). All quantitative data were assessed for normality using the Shapiro–Wilk function (the normality test resulted in p-values > α) and Identify outliers' function (ROUT method, Q = 1%; no outlier was detected) in GraphPad. One-way ANOVA with Tukey's multiple comparisons was used for positive cell bodies, expression time-course analysis, and axon density. Unpaired two-tailed Student's t-test was used for analyzing anatomical position and ratio of doubled-labeled cells of CSNs, RSNs, and RtSNs. Significant differences were defined at $^{*}p < 0.05$, $^{**}p < 0.01$, $^{***}p < 0.001$, and $^{****}p < 0.0001$.

3 | RESULTS

3.1 | AAV2-Retro rapidly labels lumbar-projection corticospinal, rubrospinal, and reticulospinal neurons

AAV2-retro has been reported to effectively address normal supraspinal inputs to the cervical and lumbar spinal cord (Wang et al., 2018). To test the time course of retrograde tracing capacity of AAV2-Retro in lumbar-projection supraspinal neurons, mice were unilaterally injected with AAV2-Retro-EGFP into the spinal cord at T13-vertebral level equaled to the L4 spinal segment. The brains and spinal cords were removed at 1, 2, 3, and 4w after injection. $EGFP^+$ CSNs, RMC and RPC populations of the red nucleus, and RtSNs were imaged in the rostral-caudal axis according to their anatomical position. Consistent with retrograde transporting to projection neurons, as previous studies reported (Tervo et al., 2016; Wang et al., 2018), AAV2-Retro rapidly transduces each supraspinal population within 1w after injection (Figure 1a,c,e,g). The number of $EGFP^+$ cells did not significantly increase from 1w to 4w (Figure 1b,d,f,h). To outline the time course of EGFP expression in axon fibers after lumbar injection, we quantitatively analyzed the mean fluorescence intensity of positive CST fibers in the cervical dorsal funiculus, which required at least 4 weeks to achieve the appropriate expression level (Figure 1i,j). These data suggest that AAV2-Retro can rapidly retrograde target lumbar-projection CSNs, RMC, PRC, and RtSNs within 1w, and fluorescent signals of these descending tracts are sufficient to be analyzed in the spinal cord within 4w.

In addition to the anatomical structure observation, layer markers (Ctip2 for layer V and Foxp2 for layer VI) and anterograde BDA tracing were performed to identify $EGFP^+$ CSNs and axons. Since layer V neurons express Ctip2, we observed co-expression of EGFP and Ctip2 signals in cell bodies (Figure 2a,b). Consistent with previous CST tracing studies (Ito et al., 2018; Ueno et al., 2018), the main BDA^+ and $EGFP^+$ CST fibers were matched in the dorsal funiculus of the thoracic spinal cord (Figure 2c,d). These results suggest that AAV2-Retro can be used to demonstrate lumbar-projection CST fibers correctly.

3.2 | AAV2-Retro maps normal supraspinal inputs to the thoracic (T9-vertebral) and lumbar (T13-vertebral) spinal cord

Understanding normal circuits rostral and caudal to T10 level is necessary to promote the relay mechanism between grafted cells and spared host neurons and circuits. To map supraspinal inputs to the thoracic (T9-vertebral) and lumbar (T13-vertebral) spinal segments, T9-vertebral and T13-vertebral level injections were performed separately. AAV2-Retro-mCherry was injected unilaterally into the spinal cord at the T9-vertebral level and AAV2-Retro-EGFP at the T13-vertebral level. Four weeks after injection, a series of 60-μm brain coronal sections were imaged. We observed contralateral projection of CSNs, and the majority of T9-vertebral and T13-vertebral projection CSNs occupy a restricted caudomedial cortex where the representative area of the hindlimb and part of the trunk located (Sahni et al., 2021; Tennant et al., 2011) (Figure 3a,b,f, Movie 1), unlike the locations of cervical-projection CSNs including rostral and caudal forelimb motor areas (RFA and CFA) previously reported (Ueno et al., 2018; Wang et al., 2018). Meanwhile, AAV2-Retro transduced corresponding spinal interneurons at injection sites without intermingling transduction. (Figure 3e). By separating the sensorimotor cortex into three areas from the midline to lateral (<1000, 1000–1500, 1500–2200 μm), we quantitatively analyzed the position differences of CSNs projecting to T9-vertebral and T13-vertebral levels (Figure 3c). Interestingly, the number of T9-vertebral projection CSNs was significantly higher than T13-vertebral projection in the area of <1000 μm ($p = 0.0010$), 1000–1500 μm ($p = 0.0456$) and 1500–2200 μm ($p = 0.0299$). The number of cell bodies in the <1000 μm area: 73.75 ± 9.217 (T9-vertebral projection) versus 19.25 ± 9.217 (T13-vertebral projection), in the 1000–1500 μm area: 281.5 ± 33.00 (T9-vertebral projection) versus 198.5 ± 33.00 (T13-vertebral projection), and in >1500 μm area: 229.3 ± 50.32 (T9-vertebral projection) versus 112.8 ± 50.32 (T13-vertebral projection). Next, we quantified the ratio of double-labeled CSNs ($EGFP^+$ and $mCherry^+$). The ratio of double-labeled cells in T13-vertebral projection is significantly higher than T9-vertebral projection (0.4991 ± 0.07793 versus 0.2790 ± 0.07793, $p = 0.0302$; Figure 3d). These data indicated that more cell bodies of CSNs projecting to T9-vertebral than to T13-vertebral reside in the cortical areas <1000 μm, 1000–1500 μm and 1500–2200 μm, and higher overlapped innervation of T13-vertebral projection CSNs in thoracic and lumbar cords.

To completely map the distribution pattern of the CSNs projecting to T9-vertebral and T13-vertebral, we next separated the sensorimotor cortex into panels with a 100-μm interval from the midline to lateral, then counted the number of cell bodies in each panel (6000 μm^2)

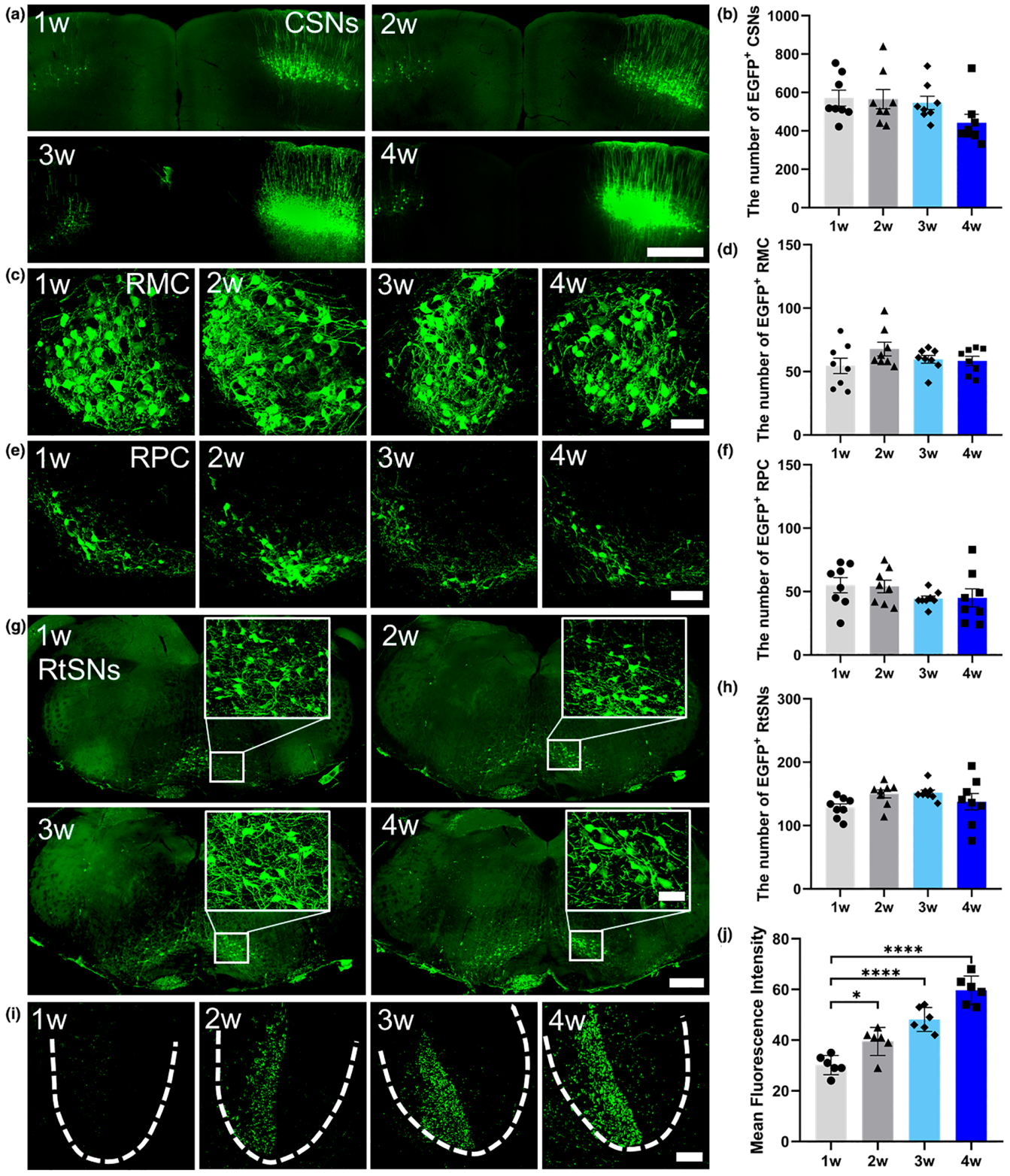

FIGURE 1 AAV2-Retro rapidly transduces CSNs, RSNs, and RtSNs after lumbar injection. AAV2-Retro-EGFP was injected unilaterally into the lumbar spinal cord (T13 vertebral level) in adult female mice. (a) CSNs were detectable within 1w. (b) Quantitation analysis of cell bodies in the contralateral sensorimotor cortex at 1, 2, 3, and 4w after injection (DF = 31, *F* value = 1.989, $p = 0.2639$). (c, e) Retrograde labeling of RSNs (RMC: magnocellular populations in (c); RPC: parvocellular populations in (e)). (d, f) Quantitative analysis of cell bodies in contralateral magnocellular (d: DF = 31, *F* value = 1.399, $p = 0.1384$; RMC) and parvocellular (f: DF = 31, *F* value = 1.120, $p = 0.3578$; RPC) areas of the red nucleus at 1, 2, 3, and 4w after injection ($p > 0.05$). (g) Retrograde labeling of RtSNs. (h) Quantitative analysis of cell bodies in ipsilateral reticular formation at 1, 2, 3, and 4w after injection (DF = 31, *F* value = 1.826, $p = 0.1654$). (i) Time course of EGFP expression in the spinal cord after lumbar injection. (j) Quantitative analysis shows a significantly increased EGFP fluorescence at 2w ($p = 0.0192$), 3w ($p < 0.0001$), 4w ($p < 0.0001$) compared to 1w (DF = 23, *F* value = 38.33, $p < 0.0001$). Scale bars: 500 μm (a, g), 100 μm (c, e, higher magnification figures in g), and 50 μm (i). $^{*}p < 0.05$, $^{****}p < 0.0001$. A one-way ANOVA with Tukey's multiple comparisons was used in b, d, f, h ($n = 8$ animals/group), and j ($n = 6$ animals/group)

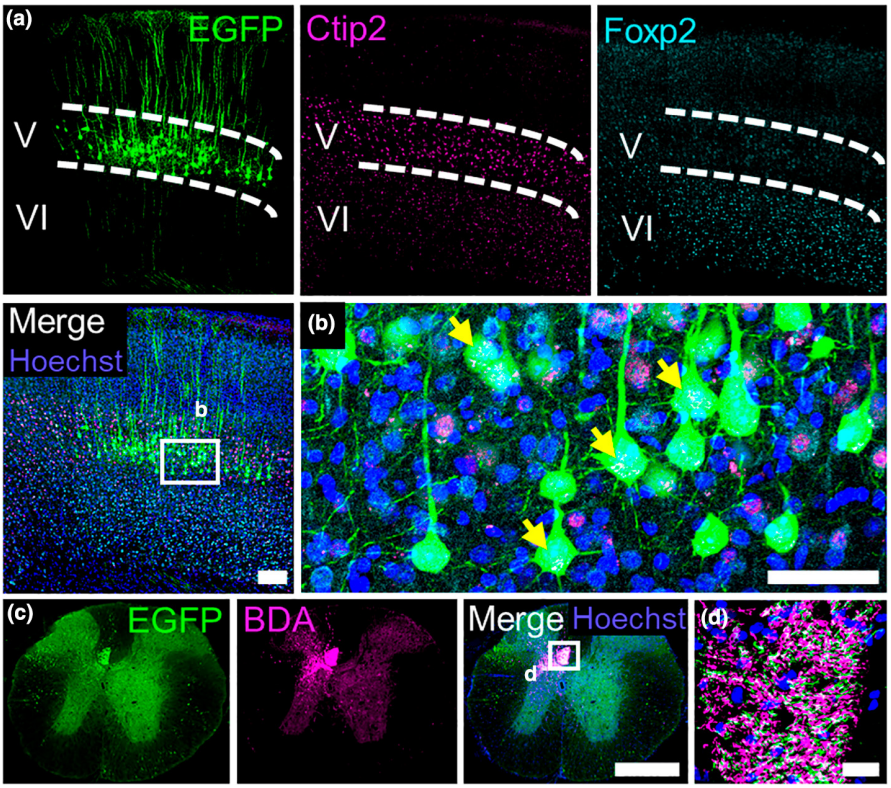

FIGURE 2 AAV2-Retro correctly transduces CSNs (layer V). (a) Representative images of immunostaining for Ctip2 and Foxp2 in coronal brain sections. (b) Enlarged image of the area in the white box in (a). Arrows show co-expression of the Ctip2 and EGFP signals. (c) Anterograde and retrograde tracing for CST. (d) High magnification image of the area in the white box in (c) shows overlapping of BDA^+ and $EGFP^+$ axon fibers in the dorsal funiculus of the thoracic spinal cord. Scale bars: 500 μm (c), 200 μm (a), 50 μm (b) and 20 μm (d)

from a complete series of 60-μm coronal sections (≈ 42 sections; $n = 3$). Subsequently, we generated a cortical distribution map (Figure 3f). The rostral edge of T9-vertebral projection CSNs was located at +0.78 mm anterior to bregma, whereas that of T13-vertebral projection CSNs was located at +0.54 mm anterior to bregma. The caudal edge of T9-vertebral projection CSNs was located at −1.2 mm posterior to bregma, whereas that of T13-vertebral projection CSNs was located at −1.08 mm posterior to bregma. Consistent with previous studies (Kamiyama et al., 2015; Wang et al., 2018), $EGFP^+$ lumbar-projection CSNs were confined to a more restricted sensorimotor cortex than the population of $mCherry^+$ thoracic-projection CSNs. Therefore, the relative location and regional number difference of CSNs show specific CST inputs between thoracic and lumbar segments.

In the red nucleus, we also observed contralateral projection of most RSNs. Next, we found the distinct distribution pattern of RSNs (RMC and RPC) projecting to T9-vertebral and T13-vertebral (Figure 3g–l). T9-vertebral and T13-vertebral projection RMC neurons were separated into two distinct populations, and the T13-vertebral projection neurons located ventrolateral to the T9-vertebral projection population with some double-labeled neurons (T9-vertebral projection: 0.3543 ± 0.08202, T13-vertebral projection: 0.3685 ± 0.08202, $p = 0.8652$; Figure 3g,h,j). Interestingly, T9-vertebral projection RPC neurons show higher cell numbers than T13-vertebral projection ($p = 0.0046$; Figure 3m). The quantification analysis of double-labeled neurons shows higher ratio in T13-vertebral projection RPC neurons than T9-vertebral projection (T9-vertebral projection: 0.1543 ± 0.09521 versus T13-vertebral projection: 0.4538 ± 0.09521, $p = 0.0104$; Figure 3n). These data suggested more cellular numbers of RPC neurons projecting to T9-vertebral than T13-vertebral in the rostral area of the red nucleus and higher overlapped innervation of T13-vertebral projection RPC neurons in thoracic and lumbar cords.

In contrast to the contralateral projection of CSNs and RSNs, we observed bilateral projection of RtSNs in reticular formation after unilateral lumbar injection as previously reported (Brownstone & Chopek, 2018; Peterson et al., 1975). The $mCherry^+$ and $EGFP^+$ RtSNs were widespread in ventral brainstem, we did not observe distribution difference ($p = 0.3479$) and ratio of double-labeled neurons (T9-vertebral projection: 0.4156 ± 0.06580 versus T13-vertebral projection: 0.5221 ± 0.06580; $p = 0.1365$) between thoracic (T9-vertebral) and lumbar (T13-vertebral) projection RtSNs (Figure 3o–r). These data suggested that T9-vertebral projection and T13-vertebral projection RtSNs are intermingled in the ventral medulla with similar overlapped connections to thoracic and lumbar cords.

Next, we observed the co-expression of EGFP and mCherry in descending axon fibers (arrows in Figure 4), which revealed that a part of supraspinal neurons innervates into both the thoracic and lumbar spinal cord. These results suggest a distinct connection pattern of CSNs, RMC, RPC, and RtSNs to thoracic and lumbar spinal segments.

3.3 | Tissue clearing and 3D imaging illustrate the spatial relationship of supraspinal inputs to thoracic (T9-vertebral) and lumbar (T13-vertebral) spinal segments

3D imaging technologies have been developed to analyze the long-range projection of neurons in intact organs (Erturk et al., 2012;

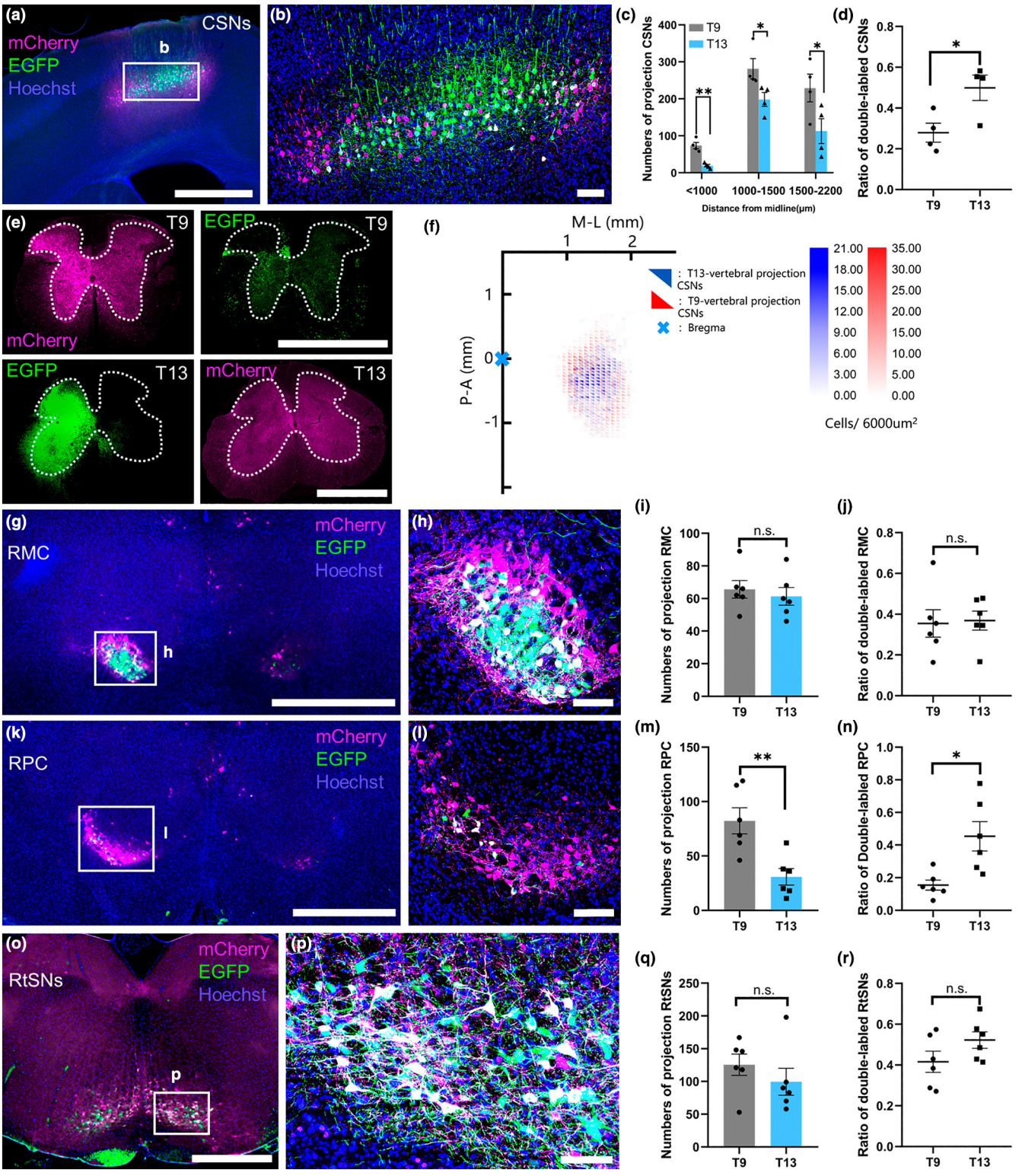

Soderblom et al., 2015). To clearly illustrate the anatomical features of supraspinal neurons and tracts, we next used modified 3DISCO and 3D reconstruction to visualize the spatial distribution of supraspinal neurons throughout the brain and spinal cord. AAV2-Retro-mCherry was bilaterally injected into the spinal cord at the T9-vertebral level and AAV2-Retro-EGFP at T13-vertebral. All images were captured based on AAV-transduced fluorescence proteins without antibody-mediated signal amplification. Consistent with the 2D section-based findings discussed above, 3D whole-brain imaging revealed global spatial organizations of supraspinal neurons projecting to the thoracic and lumbar spinal cord.

In the cerebral cortex, 3D reconstruction clarified the distribution of T9-vertebral and T13-vertebral projection CSNs in a restricted area corresponding to the primary sensorimotor cortex (Figure 5a,b; Movie 1), unlike cervical-projection CSNs with three distinct groups (a large central mass in primary sensorimotor cortex,

FIGURE 3 AAV retrograde tracings show distinct and overlapped connections of supraspinal neurons to the T9-vertebral and T13-vertebral levels. AAV2-Retro-mCherry/EGFP were unilaterally injected into the spinal gray matter at T9-vertebral and T13-vertebral levels, and the brains were analyzed after 4w. (a, b) CSNs projecting to T9-vertebral and T13-vertebral show a different distribution in the cortex (<1000, 1000–1500, and 1500–2200 μm lateral to the midline). (c) Quantitative analysis of the number of contralateral CSNs shows that the T9-vertebral projection CSNs have significantly higher cell numbers than the T13-vertebral projection CSNs in the areas <1000 μm (DF = 6, *t* value = 5.913, $p = 0.0010$), 1000–1500 μm (DF = 6, *t* value = 2.515, $p = 0.0456$), and 1500–2200 μm (DF = 6, *t* value = 2.315, $p = 0.0299$). (d) Quantification shows the ratio of double-positive CSNs with EGFP and mCherry (DF = 6, *t* value = 2.825, and $p = 0.0302$). (e). Fluorescence at injection sites after unilateral AAV injection. The dashed lines show the edge of gray matter. (f) Cortical map for mCherry and EGFP labeled CSNs. Gradation of color in each triangle means cell number. (g–n) Representative images in the midbrain show a different distribution of the magnocellular (RMC; g, h) and parvocellular (RPC; k, l) populations of the red nucleus. (i) Quantitative analysis shows similar numbers of RMC projecting to T9-vertebral and T13-vertebral (DF = 10, t value = 0.5669, and $p = 0.5833$). (j) Quantification shows the ratio of double-positive RMC neurons with EGFP and mCherry (DF = 10, *t* value = 0.1742, and $p = 0.8652$). (m) Quantitative analysis shows that the T9-vertebral projection RPC has significantly more cell bodies than the T13-vertebral projection (DF = 10, *t* value = 3.627, and $p = 0.0046$). (n) Quantification shows the ratio of double-positive RPC neurons with EGFP and mCherry (DF = 10, *t* value = 3.145, and $p = 0.0104$). (o, p) Representative images in the brainstem show a similar distribution of RtSNs projecting to T9-vertebral and T13-vertebral. (q) Quantitative analysis of the number of ipsilateral RtSNs shows similar cell numbers of T9-vertebral versus T13-vertebral projection RtSNs (DF = 10, *t* value = 0.9849, and $p = 0.3479$). (r) Quantification shows the ratio of double-positive RtSNs (DF = 10, *t* value = 1.619, and $p = 0.1365$). Scale bars: 1000 μm (a, e, g, k, o) and 100 μm (b, h, l, p). $^{*}p < 0.05$, $^{**}p < 0.01$, $^{****}p < 0.0001$; n.s., not significant. Statistical analysis was performed using an unpaired two-tailed Student's *t*-test in c, d ($n = 4$ animals), f ($n = 3$ animals), and i, j, m, n, q, r ($n = 6$ animals)

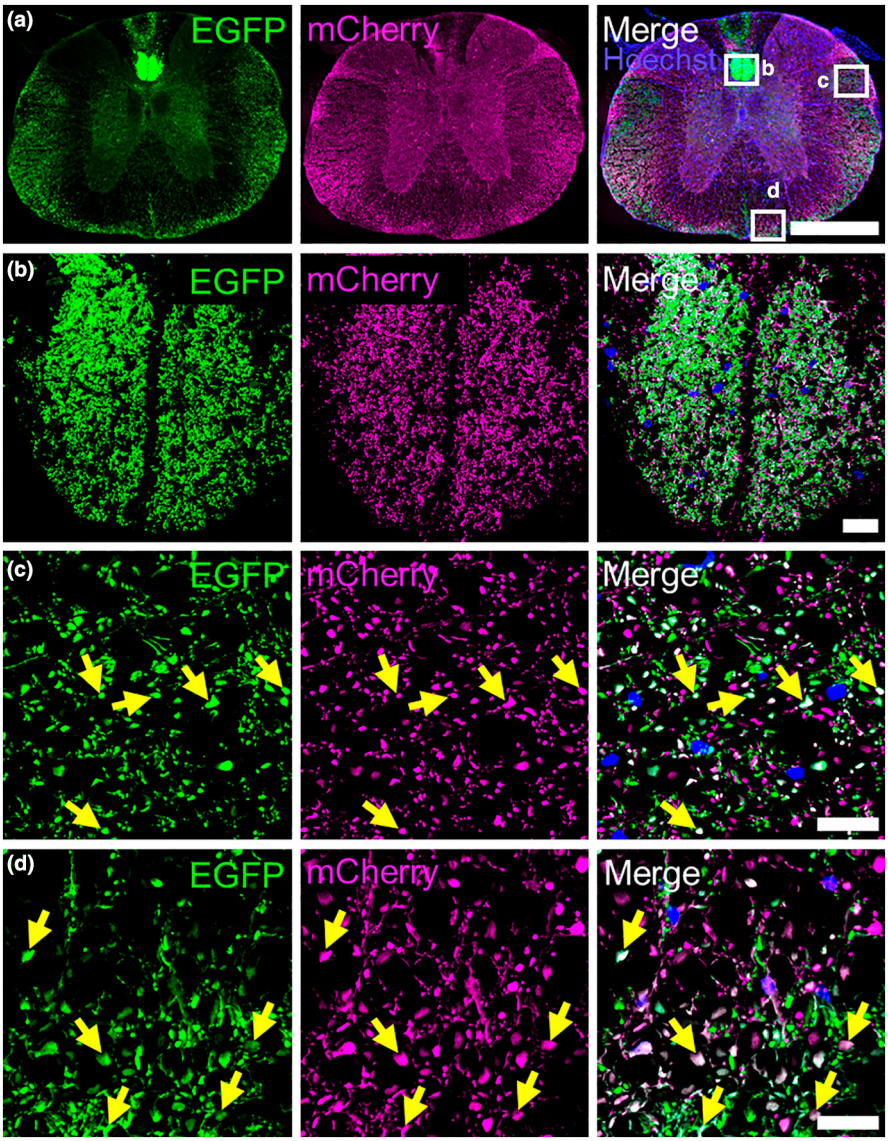

FIGURE 4 AAV tracings from T9-vertebral and T13-vertebral show descending tracts in the upper thoracic spinal cord. AAV2-Retro- mCherry/EGFP were bilaterally injected into the spinal cord at T9-vertebral and T13-vertebral levels, and after 4w, the spinal cords were analyzed. (a) Axial sections show the distribution of axon fibers of supraspinal neurons projecting to T9-vertebral and T13-vertebral levels. High-magnification images (white boxes in (a)) show the CST in the dorsal funiculus (b), the RST, and dorsolateral CST in the dorsolateral white matter (c) and the RtST and some propriospinal axons in the ventral white matter (d). Yellow arrows show the colocalization of mCherry and EGFP in the axons. Scale bars: 500 μm (a) and 20 μm (b–d)

a particular group in RFA, and a caudal/lateral group in secondary sensory cortex) (Wang et al., 2018). Interestingly, more double-labeled (T9-vertebral projection: 0.2790±0.07793, T13-vertebral projection: 0.4991±0.07793; Figure 3d) cell bodies were observed in these projection neurons compared to a previous retrograde tracing study focused on cervical-projection and lumbar-projection CSNs, which reported only a few double-labeled neurons (Steward et al., 2021).

Similarly, 3D visualization of the red nucleus showed the spatial position of parvocellular (RPC, rostral) and magnocellular (RMC, caudal) populations and differences in cell morphology as indicated by the anatomical nomenclature (Figure 5c,d; Movie 1). T9-vertebral versus T13-vertebral projection RMC neurons were separated into two distinct populations. The T13-vertebral projection cell bodies were located ventrolateral to the T9-vertebral projection population with some double-labeled neurons (T9-vertebral projection: 0.3543±0.08202, T13-vertebral projection: 0.3685±0.08202; Figure 3j and Figure 5d–d). Interestingly, T9-vertebral projection RPC neurons show more cell numbers and a lower ratio of double-labeling than the T13-vertebral projection (T9-vertebral projection: 0.1543±0.09521, T13-vertebral projection: 0.4538±0.09521; Figure 3n and Figure 5d–d').

In the brainstem, RtSNs projecting to T9-vertebral and T13-vertebral were widespread in the ventral medulla without significant differences in the number and double-labeled ratio (T9-vertebral projection: 0.4156±0.06580, T13-vertebral projection: 0.5221±0.06580; Figure 3r and Figure 5a). 3D imaging also helped map the relationship between reticulospinal neurons and the pyramidal tract (Figure 5e,f and Movie 1).

Overall, 3D reconstruction provides an integrated connection difference of the supraspinal projections in the brain between the thoracic and lumbar spinal cord.

3.4 | Cre-DIO system outlines axon collateral networks of single-segment projection CSNs (T9-vertebral projection or T13-vertebral projection)

The disagreement of double-labeled neurons has been reported in previous studies using retrograde tracing to target cervical and lumbar-projection CSNs (Kamiyama et al., 2015; Steward et al., 2021; Wang et al., 2018). Although these double-labeled neurons indicated that certain CSNs innervate both the cervical and lumbar spinal cord (Kamiyama et al., 2015; Steward et al., 2021), the distribution of the axon terminals of projection CSNs in spinal cords is still unclear. Since substantial collateral branches of CST have been demonstrated, which innervate in various brain regions (Frezel et al., 2020; Wang et al., 2018), we hypothesized that the axon branches of spinal-projection CSNs are distributed in different levels of spinal gray matter, which probably mediated the uptake of viral particles in the spinal segment at T9-vertebral and T13-vertebral levels. To clarify the collateralization of CSNs projecting to a single spinal segment, we precisely labeled projection CSNs using the Cre-DIO system. AAV2-DIO-EGFP was bilaterally injected into the sensorimotor

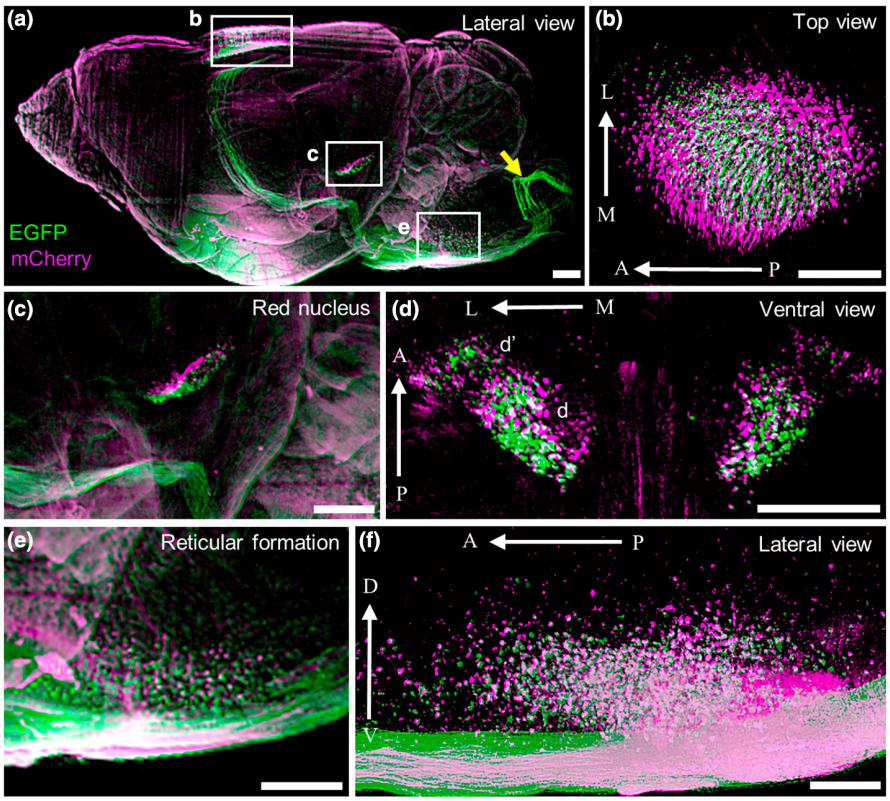

FIGURE 5 3D imaging reveals supraspinal neurons and descending tracts. (a–f). AAV2-Retro-mCherry/EGFP were injected bilaterally into the spinal cord at T9-vertebral and T13-vertebral levels, and 4 weeks later, the brains were cleared by modified 3DISCO and imaged with light-sheet microscopy. (a–f) The lateral view of the 3D reconstruction for the right brain hemisphere shows the spatial relationship of CSNs (b), RSNs (c, d), and RtSNs (e, f) projecting to T9-vertebral and T13-vertebral levels. (b, c, e) High magnification images of the area in white boxes in (a). (m–l): midline to lateral; a–p: anterior to posterior; d–v: dorsal to ventral. (d, f) High magnification images of neurons shown in (c, e). (d') the red nucleus's RPC and RMC populations (d). Videos are available as supplementary movies. Scale bars: 500 μm (a–e) and 200 μm (f)

cortex and AAV2-Retro-pgk-Cre into the spinal cord at T9-vertebral or T13-vertebral level.

Four weeks after injection, cell bodies and tracts were successfully labeled (T9-vertebral projection: Figure 6a,b; T13-vertebral projection: Figure 7a,b). Consistent with previous studies (Wang et al., 2017; Wang et al., 2018), the main tract of CST descends through the cerebral peduncle and ventral medulla, as shown by yellow arrows (Figure 6&7C–F). Interestingly, in addition to the main tracts, abundant axon collaterals of T9-vertebral or T13-vertebral projection CSNs innervated in the red nuclei (Figure 6 and 7C,D and Movie 2) and reticular formation (Figure 6 and 7E,F; Movie 2), which indicated complex neuronal communications among motor control centers in normal motor execution. Furthermore, we next observed that many axon branches ($EGFP^+$) are located in gray matter from the cervical to lumbar spinal cord (Figure 6 and 7 G–S). Therefore, these results indicate that the CST collaterals from single spinal segment projection CSNs spread extensively throughout the brain and spinal cord.

In the cervical enlargement, the axons of T9-vertebral or T13-vertebral projection neurons mainly innervated in the medial gray matter (Figure 6g–j and Figure 7g–j), which is different from the sensory corticospinal axons (mainly innervated in dorsal spinal gray regions) previously described (Gu et al., 2019). In the middle thoracic segments, the distribution pattern of axons is different between T9-vertebral and T13-vertebral projection CSNs. The percentages of axons from T9-vertebral projection CSNs in the dorsal and medial gray matter are significantly higher than in the ventral region (dorsal versus ventral: $p = 0.0212$, medial versus ventral: $p = 0.0097$; Figure 6o). In contrast, only the percentage of axons in medial gray matter is significantly higher than the ventral region ($p = 0.0218$; Figure 7o) in T13-vertebral projection CSNs, while similar percentages between dorsal versus medial regions ($p = 0.0576$) and ventral parts are observed ($p = 0.7097$); Figure 7o). In the lumbar enlargement, the axons from T13-vertebral projection CSNs mainly innervated in the dorsal region (dorsal versus ventral: $p = 0.0013$, dorsal versus medial: $p = 0.0368$; Figure 7s), whereas the innervation of T9-vertebral projection CSNs was similar in dorsal and medial gray matter ($p = 0.6762$; Figure 6s). Consistent with previous studies (Gu et al., 2019) and heatmap of EGFP+ axon terminals in gray matter (Figure S1), the axons in ventral gray matter show less innervation than the dorsal (T9-vertebral projection: $p = 0.0016$; T13-vertebral projection: $p = 0.0013$) and medial (T9-vertebral projection: $p = 0.0034$; T13-vertebral projection: $p = 0.0324$) regions (Figure 6 and Figure 7S). Overall, these results demonstrate the complexity of collateral branches of single thoracic or lumbar spinal projection CSNs.

Since layer V neurons express vGLUT1 (Fremeau et al., 2001), we used it to target CST synaptic terminals of T9-vertebral projection or T13-vertebral projection CSNs. Our results showed that the $EGFP^+$ terminals co-localized with vGLUT1 in the red nucleus (Figure S2c,d) and reticular formation (Figure S2g,h). In the cervical spinal cord, we observed that the $EGFP^+$ synaptic terminals in intermediate gray matter co-localized with vGLUT1 (Figure S3, arrows).

3D imaging and Cre-DIO system revealed positive cell bodies projecting to thoracic (T9-vertebral) or lumbar (T13-vertebral) segment in the primary sensorimotor cortex, as well as their tracts descending into the midbrain and ventral medulla (Figure 8a,g; Movie 3). High magnification images illustrated that many axon branches from main CST tracts innervate into other brain regions, as yellow arrows are shown (T9-vertebral projection: Figure 8c–f; T13-vertebral projection: Figure 8i–l), and axon terminals in red nucleus (arrows; Figure 8e) and reticular formation (arrows; Figure 8k,l).

4 | DISCUSSION

This study highlights the difference in connectivity of the thoracic (T9-vertebral level) and lumbar (T13-vertebral level) projection supraspinal neurons. We demonstrated distinct anatomical distributions and ratios of double-labeled supraspinal neurons in the sensorimotor cortex, red nucleus, and reticular formation. 3D imaging and reconstruction provided the anatomical difference of supraspinal neurons between the thoracic and lumbar projection. Finally, the intersectional strategy revealed abundant collateral branches of CSNs projecting to a single spinal segment throughout the brain and spinal cord, which confirmed the complex collateralization of single-segment projection CSNs. These findings map the brain-spinal inputs to the thoracic and lumbar spinal cord and clarify the innervation pattern of thoracic or lumbar projection CSNs.

4.1 | Rapid and correct retrograde labeling for supraspinal neurons

AAV2-Retro, which was developed using a directed-evolution approach, allows efficient retrograde transport to neuronal somas projecting to the injection site in the brain (Tervo et al., 2016) and spinal cord (Wang et al., 2018). In particular, high transduction in CSNs makes it prominent compared to other AAV serotypes (Matsuzaki et al., 2017; Sheikh et al., 2018; Sun et al., 2019). Consistent with these studies, we confirmed the powerful retrograde labeling capacity of AAV2-Retro for spinal projection CSNs, RSNs, and RtSNs within 1w after lumbar injection. Furthermore, we quantified AAV-transduced fluorescence, which is suitable for detection within 4w. These results indicated a rapid capacity of AAV2-Retro for retrograde access to long-range supraspinal neurons.

In layer V of the primary sensorimotor cortex, CSNs project axons to the spinal cord, which is the most important voluntary motor system (Oswald et al., 2013). We previously used BDA anterograde tracing to study spared CST fibers after SCI in LOTUS-Tg mice (Ito et al., 2018). To guarantee correct labeling for CSNs, we performed immunostaining of layer V antibody and anterograde BDA tracing for CST. Our results showed colocalization of EGFP and Ctip2 signals in cell bodies and colocalization of $EGFP^+$ and BDA^+ CST axon fibers at the dorsal funiculus of spinal white matter (Ito

Journal of Neurochemistry JNC The Official Journal of the International Society for Neurochemistry WILEY

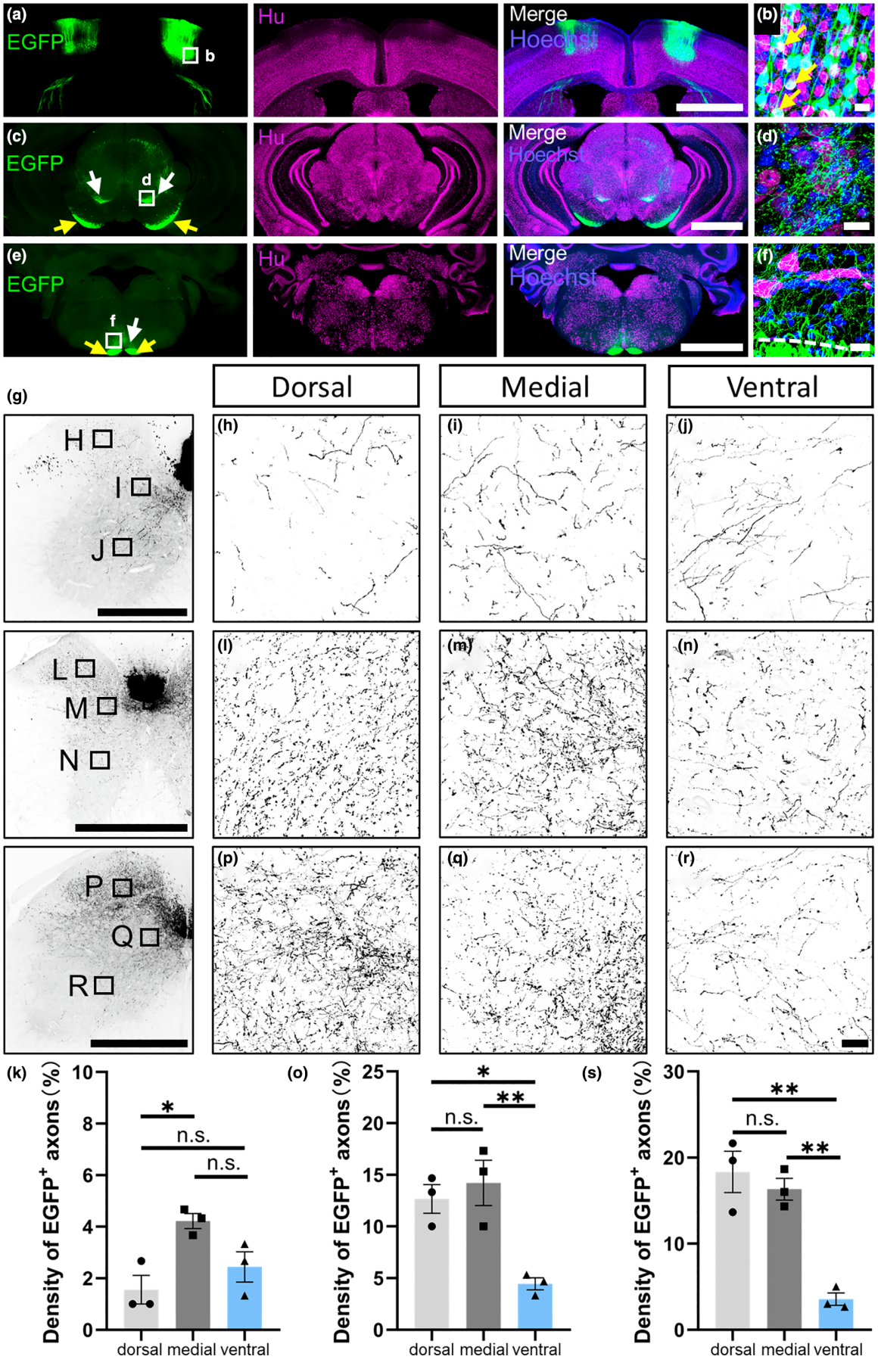

FIGURE 6 Collateralization of T9-vertebral projection CSNs throughout the brain and spinal cord. AAV2-DIO-EGFP was injected bilaterally in the cortex, while AAV2-Retro-pgk-Cre was injected bilaterally into the spinal cord at the T9-vertebral level. (a, b) Representative images of labeled CSNs. Hu antibody was used to label neurons. Arrows in (b) show co-expression of EGFP and Hu. (c, d) Representative images of axon collaterals of T9-vertebral projection CSNs innervated in red nuclei (white arrows shown). Yellow arrows show CST fibers in the cerebral peduncle. (e, f) Representative images of axon branches of T9-vertebral projection CSNs innervated in the reticular formation (white arrows shown). The yellow arrows show the main tracts of the CST. The dashed line in (f) shows the area of the pyramidal tract. (g–s) Axial views show the axon terminals of T9-vertebral projection CSNs in spinal gray matter. Representative images of axon branches in the gray matter of cervical enlargement (h–j), middle thoracic (l–n), and lumbar enlargement (p–r). (k) Quantitative analysis of axon density in cervical gray matter shows that innervation in the medial area is more pronounced than in the dorsal area ($p = 0.0211$) and similar to the ventral area ($p = 0.0983$) (DF = 8, F value = 7.47, $p = 0.0235$). (o) Quantitative analysis of axon density in thoracic gray matter shows significantly more distribution in the dorsal ($p = 0.0212$) and medial areas ($p = 0.0097$) than in the ventral area (DF = 8, F value = 11.73, $p = 0.0085$). (s) Quantitative analysis of axon density in lumbar gray matter shows a significantly greater distribution in the dorsal ($p = 0.0016$) and medial areas ($p = 0.0034$) than in the ventral area (DF = 8, F value = 24.40, $p = 0.0013$). Scale bars: 2 mm (a, c, e), 500 μm (g), and 20 μm (b, d, f, h–r). $^{**}p < 0.01$, $^{****}p < 0.0001$; n.s., not significant. A one-way ANOVA with Tukey's multiple comparisons was used in (k, o, s) (3 confocal image stacks per animal, $n = 3$ animals/group)

et al., 2018); these data further confirmed correct transduction of AAV2-Retro for CSNs.

4.2 | Clarification of supraspinal inputs to the thoracic and lumbar spinal cord

Thoracic SCI models have been widely used to develop therapeutic strategies for patients with SCI. Other groups and we have confirmed that the formation of synapses between grafted hiPSCs-derived neurons and host-spared neurons, relaying circuits rostral and caudal to the lesion, promoted hindlimb motor function and electrophysiological recovery in T10-SCI mice (Fandel et al., 2016; Nori et al., 2011; Okubo et al., 2016; Okubo et al., 2018; Ropper et al., 2017). Generally, anterograde BDA tracing is used to evaluate the axonal regeneration of the descending pathway after stem cell transplantation (Kadoya et al., 2016; Kumamaru et al., 2019). However, little is known about normal supraspinal inputs to thoracic (rostral to the lesion) and lumbar (below lesion) spinal levels (Ferreira-Pinto et al., 2018; Moreno-Lopez et al., 2021). One limitation of anterograde tracing is the imprecise labeling for specific site projections. For clarifying these inputs to the spinal cord, retrograde tracing is necessary. AAV2-Retro was injected separately in the thoracic (mCherry) and lumbar (EGFP) spinal segments. As discussed above, our data mapped the difference in connectivity of the CSNs, RMC, RPC, and RtSNs that project to the thoracic and lumbar cords. In the sensorimotor cortex, T9-vertebral and T13-vertebral projection CSNs were confined to the primary sensorimotor cortex, which is different from CSNs projecting to the cervical spinal cord (RFA, CFA, and caudal/lateral group in the secondary sensory cortex) as previously reported (Ueno et al., 2018; Wang et al., 2017). Furthermore, the range of T9-vertebral projection CSNs is located broader than T13-vertebral projection CSNs, and more cells in the medial and lateral areas. In the caudal region of the red nucleus, most of the magnocellular (RMC) populations projecting to the T13-vertebral level are located in the ventrolateral region and neurons projecting to T9-vertebral at dorsomedial region. Some double-labeled neurons were observed in the adjacent area of them (Liang et al., 2012; Sheikh et al., 2018; Wang et al., 2018). Surprisingly, in the rostral region of the red nucleus, the number of parvocellular (RPC) populations projecting to the T13-vertebral is much lower than the neurons projecting to the T9-vertebral level. Meanwhile, most of the T13-vertebral projection RPC neurons are located in the ventrolateral area. In contrast to the specific distribution pattern of CSNs, RMC, and RPC, the T9-vertebral and T13-vertebral projection RtSNs are intermingled in the ventral medulla with similar distribution positions.

Different transduction capacities among other promoters of the AAV virus have been reported previously (Haenraets et al., 2017). These authors found that intraspinal injection of AAV9.hSyn1.EGFP led to a significantly reduced number of positive cell bodies in the dorsal root ganglia neurons (DRGs) compared with AAV9.CAG.EGFP. This different transduction capacity between CAG and hSyn1 promoters may explain why populations in the upper medulla and pons are not labeled (hSyn in our study; CAG in Wang et al., 2018).

Notably, we observed more double-labeled CSNs (thoracic- versus lumbar-projection) than previous reports studied on cervical- versus lumbar-projecting (T12 and L4 spinal segments in our study; C7 and L4 spinal segments in Kamiyama et al., 2015; C5 and L2 spinal segments in Steward et al., 2021). On the contrary, Wang et al, (2018) did not observe any double-labeled CSNs and RSNs after intraspinal injection of AAV2-Retro-CAG-tdTomato into the spinal segment between L3 and L4 vertebrae and AAV2-Retro-CAG-EGFP into the spinal segment between C4 and C5 vertebrae. These results indicated a higher overlapping innervation of corticospinal and rubrospinal inputs to the thoracic and lumbar spinal cord than to the cervical and lumbar spinal cord.

Our previous works reported that the grafted cells migrated rostrally and caudally in mice (Ishii et al., 2006; Ito et al., 2021; Kawai et al., 2021; Kitagawa et al., 2022) and marmoset (Iwanami et al., 2005), which increased the connection between grafted cell-derived neurons and host spared interneurons and fibers around lesion area. Although the tendency of circuit formation between grafted cells and rostral thoracic-projection or lumbar-projection supraspinal neurons as well as which way contributes more function recovery needs to be further studied, this work provided a kind of anatomical distribution

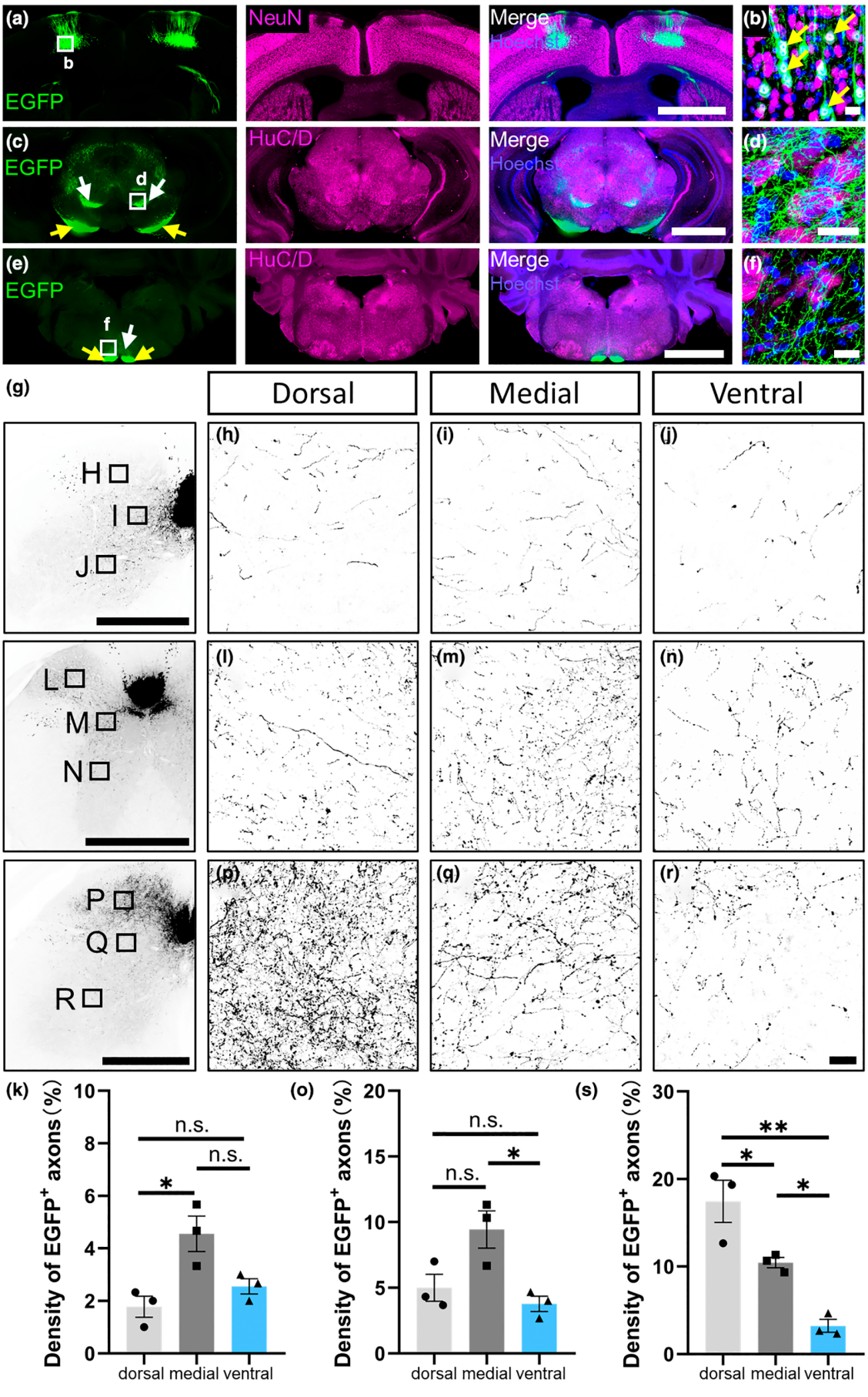
(a)
b
EGFP
NeuN
Merge
Hoechst
(b)
(c)
EGFP
d
HuC/D
Merge
Hoechst
(d)
(e)
EGFP
f
HuC/D
Merge
Hoechst
(f)
(g)
Dorsal
Medial
Ventral
H
I
J
(h)
(i)
(j)
L
M
N
(l)
(m)
(n)
P
Q
R
(p)
(q)
(r)
(k)
Density of EGFP+ axons (%)
n.s.
n.s.
*
dorsal medial ventral
(o)
Density of EGFP+ axons (%)
n.s.
*
n.s.
dorsal medial ventral
(s)
Density of EGFP+ axons (%)
**
*
*
dorsal medial ventral

FIGURE 7 Collateralization of T13-vertebral projection CSNs throughout the brain and spinal cord. AAV2-DIO-EGFP was bilaterally injected into the cortex, while AAV2-Retro-pgk-Cre was bilaterally injected into the spinal cord at the T13-vertebral level. (a, b) Representative images of labeled CSNs. NeuN and HuC/D were used to label neurons. Arrows in (b) show the co-expression of EGFP and NeuN. (c, d) Representative images of axon collaterals of T13-vertebral projection CSNs innervated in red nuclei (white arrows shown). Yellow arrows show CST fibers in the cerebral peduncle. (e, f) Representative images of axon branches of T13-vertebral projection CSNs innervated in the reticular formation (white arrows). The yellow arrows show the main tracts of the pyramidal tract. (g–s) Axial views show axon terminals of T13-vertebral projection CSNs in spinal gray matter. Representative images of axon branches in the gray matter of cervical enlargement (h–j), middle thoracic (l–n), and lumbar enlargement (p–r). (k) Quantitative analysis of axon density in cervical gray matter shows significantly more innervation in the medial area ($p = 0.0157$) than the dorsal area (DF = 8, F value = 8.754, $p = 0.0166$). (o) Quantitative analysis of axon density in thoracic gray matter shows significantly more innervation in the medial area ($p = 0.0218$) than in the ventral area (DF = 8, F value = 7.858, $p = 0.0211$). (s) Quantitative analysis of axon density in lumbar gray matter shows significantly more innervation in the dorsal than in medial ($p = 0.0368$) and ventral areas ($p = 0.0013$), as well as medial vs. ventral ($p = 0.0324$) (DF = 8, F value = 22.76, $p = 0.0016$). Scale bars: 2 mm (a, c, e), 500 μm (g), and 20 μm (b, d, f, h–r). $^{*}p < 0.05$, $^{**}p < 0.01$, $^{***}p < 0.001$, $^{****}p < 0.0001$; n.s., not significant. A one-way ANOVA with Tukey's multiple comparisons was used in (k, o, s) (3 confocal image stacks per animal, $n = 3$ animals/group)

pattern of supraspinal inputs to rostral and caudal spinal segments, which mapped the relative location of CSNs and RNs projecting to T9-vertebral (rostral) and T13-vertebral level (caudal).

A reasonable concern is the specificity of AAV2-Retro uptake and retrograde transport by axon terminals versus pathways. In this study, to minimize the off-target problem, our injection coordinates in the spinal cord have already avoided the main tracts in spinal white matter.

4.3 | Intersectional viral strategy precisely revealed the complexity of the collateral network of CSNs projecting to a single spinal segment

Double-labeled CSNs were shown in two retrograde tracing studies with cervical and lumbar injection (Kamiyama et al., 2015; Steward et al., 2021), a study with cervical and thoracic injection (Ghosh et al., 2010). However, an unanswered question in neural circuit tracing is related to the distribution pattern of the axon collaterals from specific spinal projection CSNs. Ghosh et al. discussed that double-labeled hindlimb CSNs traced by different fluorescent chemical tracers have fibers projected to the cervical and lower thoracic or lumbosacral cord. However, these authors did not show detailed collateral branches in the corresponding regions of the spinal cord. In other studies, anterograde tracing was used mainly to label CST and its branches in the spinal cord (Liu et al., 2018; Steward et al., 2021; Ueno et al., 2018; Wang et al., 2017). However, this strategy lacks the precision required to study the collateral networks of CSNs projecting to a single segment of the spinal cord. Using a Cre-dependent expression system, the intersectional viral approach is useful for precisely targeting projection neurons with minimum off-target labeling for other tracts. We specifically labeled CSNs projecting to the T9-vertebral or T13-vertebral level using the Cre-DIO system. Their widespread axon branches were observed in other brain regions and spinal cord regions rather than limited to the injection site, which clearly explained why the viral particles injected in different spinal segments, were retrogradely transported to the same cell bodies.

Furthermore, the distribution pattern of axon branches from CSNs projecting to a single spinal segment shows different innervation of CSNs in dorsal spinal gray matter, especially in thoracic and lumbar spinal cords. This difference could suggest the more spinal segment-specific manner of sensory-related CST fibers (Ueno 2018; Liu Nature 2018) than ventral motor-related axons. Thus, this work provided a definite brain-spinal map for the complex collateralization of single thoracic or lumbar segment projection CSNs.

In this study, one limitation of 3D imaging is the lack of quantitative analysis of positive neurons. With the development of machine learning methods, deep learning-assisted image analysis is a suitable tool for fully automated registration and quantification of tyrosine hydroxylase positive neurons (Roostalu et al., 2019). However, its application for quantifying the cell numbers of projection neurons still needs to be tested in the future. Brainrender provides another possibility for later work (Blackmore et al., 2021; Claudi et al., 2021). Another limitation is the lack of functional dissection for T9-vertebral and T13-vertebral projection supraspinal neurons in the mouse model. The chemogenetic and optogenetic strategies would be optimal tools for dissecting function control of each supraspinal neuron, as previously demonstrated (Kamiyama et al., 2015; Wang et al., 2018). An appropriate animal model, such as a marmoset, is also needed to achieve this goal, as we previously demonstrated (Kondo et al., 2018).

In conclusion, using genetic tools and 3D imaging, our findings revealed the difference in anatomical position between thoracic and lumbar projection neurons in intact adult mice. They uncovered the axon collateral network of CSNs projecting to a single spinal segment. This study highlights the connectivity of the brain-spinal cord neural network that could promote the development of more specific therapeutic strategies and the complexity of axon terminals of spinal projection CSNs, which could contribute to the development of targeted therapeutic strategies connecting CST fibers and hindlimb function recovery.

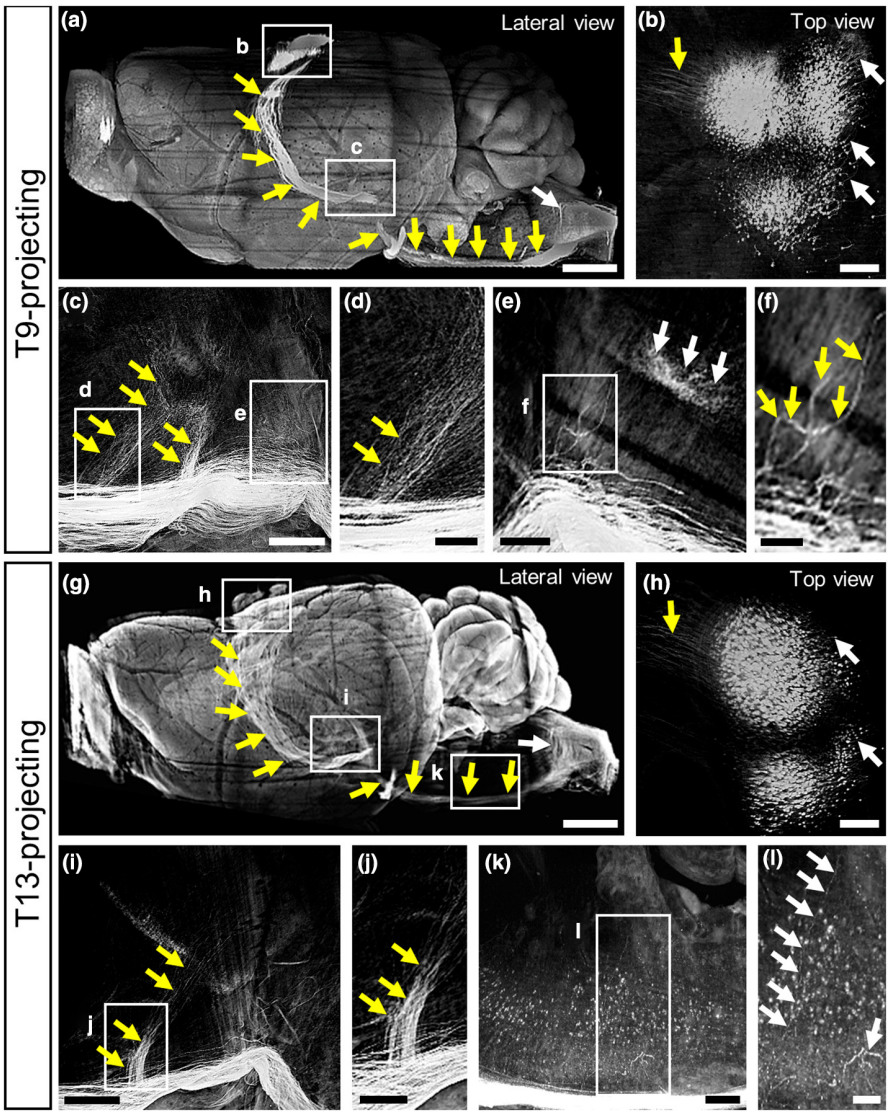

FIGURE 8 3D reconstruction of the axon collateral network of CSNs projecting to T9-vertebral or T13-vertebral level. (a–f) 3D images show the main CST tracts and the axon collaterals of T9-vertebral projection CSNs. (a) Lateral view shows that EGFP$^+$ CST fibers originate in the cerebral cortex, descend ventrally into the midbrain, medulla (yellow arrows), then through the dorsal medulla into the spinal cord (white arrow). (b) Top view of EGFP$^+$ soma, dendrites (white arrows), and descending axons (yellow arrow). (c–f) High magnification images of collateral branches from the main CST tract (yellow arrows) and axon terminals innervate into the red nuclei (white arrows). (g–l) 3D images show the main CST tracts and axon collaterals of T13-vertebral projection CSNs. (g) The lateral view shows that EGFP$^+$ CST fibers originate in the cerebral cortex, descend ventrally into the midbrain, and medulla (yellow arrows), then circulate through the dorsal medulla into the spinal cord (white arrow). (h) Top view of EGFP$^+$ soma, dendrites (white arrows), and descending axons (yellow arrow). (i–l) High magnification images of collateral branches from the main CST tract (yellow arrows) and axon terminals innervate into reticular formation (white arrows). Scale bars: 1 mm (a, g), 200 μm (b, c, h, i, k), 100 μm (d, e, j, l), and 50 μm (f)

AUTHOR CONTRIBUTIONS

T. L., M.S., M.N., and H.O. designed this project; T. L. and M.S. performed experiments. T. L., M.S., N.N. analyzed data. T. L., M.S., N.N., M.N., and H.O. interpreted and wrote the manuscript. M.N. and H.O. supported and supervised this project. All authors approved the final manuscript.

ACKNOWLEDGMENTS

This research was supported by the Japan Agency for Medical Research and Development (AMED) (Number JP20bm0204001, JP19bm0204001, and JP18bk0104017 to H.O. and M.N.) and supported by Japan Science and Technology Agency (JST) SPRING, Grant Number JPMJSP2123 (To T.L.). We thank Dr. T. Kondo, Y. Sato, for the technical support on virus injection.

All experiments were conducted in compliance with the ARRIVE guidelines.

CONFLICT OF INTEREST

H.O. is a compensated scientific consultant at San Bio Co. Ltd., and K Pharma Inc. M.N. is a consultant scientist at K Pharma Inc. The other authors declared no competing financial interests.

DATA AVAILABILITY STATEMENT

The data supporting this study's findings are available from the corresponding author upon reasonable request.

ORCID

Tao Lu https://orcid.org/0000-0002-3334-8279
Munehisa Shinozaki https://orcid.org/0000-0002-1116-2713
Narihito Nagoshi https://orcid.org/0000-0001-8267-5789
Masaya Nakamura https://orcid.org/0000-0002-2279-7028
Hideyuki Okano https://orcid.org/0000-0001-7482-5935

REFERENCES

Asboth, L., Friedli, L., Beauparlant, J., Martinez-Gonzalez, C., Anil, S., Rey, E., Baud, L., Pidpruzhnykova, G., Anderson, M. A., Shkorbatova, P., Batti, L., Pagès, S., Kreider, J., Schneider, B. L., Barraud, Q., & Courtine, G. (2018). Cortico-reticulo-spinal circuit reorganization enables functional recovery after severe spinal cord contusion. *Nature Neuroscience*, *21*, 576–588.

Blackmore, M., Batsel, E., & Tsoulfas, P. (2021). Widening spinal injury research to consider all supraspinal cell types: Why we must and how we can. *Experimental Neurology*, *346*, 113862.

Brownstone, R. M., & Chopek, J. W. (2018). Reticulospinal Systems for Tuning Motor Commands. *Frontiers in Neural Circuits*, *12*, 30.

Chen, C., Chen, H., Zhang, Y., Thomas, H. R., Frank, M. H., He, Y., & Xia, R. (2020). TBtools: An integrative toolkit developed for interactive analyses of big biological data. *Molecular Plant*, *13*, 1194–1202.

Claudi, F., Tyson, A. L., Petrucco, L., Margrie, T. W., Portugues, R., & Branco, T. (2021). Visualizing anatomically registered data with brainrender. *eLife*, *10*, 1–16.

Engmann, A. K., Bizzozzero, F., Schneider, M. P., Pfyffer, D., Imobersteg, S., Schneider, R., Hofer, A. S., Wieckhorst, M., & Schwab, M. E. (2020). The gigantocellular reticular nucleus plays a significant role in locomotor recovery after incomplete spinal cord injury. *The Journal of Neuroscience*, *40*, 8292–8305.

Erturk, A., Becker, K., Jahrling, N., Mauch, C. P., Hojer, C. D., Egen, J. G., Hellal, F., Bradke, F., Sheng, M., & Dodt, H. U. (2012). Three-dimensional imaging of solvent-cleared organs using 3DISCO. *Nature Protocols*, *7*, 1983–1995.

Fandel, T. M., Trivedi, A., Nicholas, C. R., Zhang, H., Chen, J., Martinez, A. F., Noble-Haeusslein, L. J., & Kriegstein, A. R. (2016). Transplanted human stem cell-derived interneuron precursors mitigate mouse bladder dysfunction and central neuropathic pain after spinal cord injury. *Cell Stem Cell*, *19*, 544–557.

Ferreira-Pinto, M. J., Ruder, L., Capelli, P., & Arber, S. (2018). Connecting circuits for supraspinal control of locomotion. *Neuron*, *100*, 361–374.

Fremeau, R. T., Troyer, M. D., Pahner, I., Nygaard, G. O., Tran, C. H., Reimer, R. J., Bellocchio, E. E., Fortin, D., Storm-Mathisen, J., & Edwards, R. H. (2001). The expression of vesicular glutamate transporters defines two classes of excitatory synapse. *Neuron*, *31*, 247–260.

Frezel, N., Platonova, E., Voigt, F. F., Mateos, J. M., Kastli, R., Ziegler, U., Karayannis, T., Helmchen, F., Wildner, H., & Zeilhofer, H. U. (2020). In-depth characterization of layer 5 output neurons of the primary somatosensory cortex innervating the mouse dorsal spinal cord. *Cerebral Cortex Communications*, *1*, 1–16.

Ghosh, A., Haiss, F., Sydekum, E., Schneider, R., Gullo, M., Wyss, M. T., Mueggler, T., Baltes, C., Rudin, M., Weber, B., & Schwab, M. E. (2010). Rewiring of hindlimb corticospinal neurons after spinal cord injury. *Nature Neuroscience*, *13*, 97–104.

Gu, Z., Ueno, M., Klinefelter, K., Mamidi, M., Yagi, T., & Yoshida, Y. (2019). Skilled movements in mice require inhibition of corticospinal axon collateral formation in the spinal cord by semaphorin signaling. *The Journal of Neuroscience*, *39*, 8885–8899.

Haenraets, K., Foster, E., Johannssen, H., Kandra, V., Frezel, N., Steffen, T., Jaramillo, V., Paterna, J. C., Zeilhofer, H. U., & Wildner, H. (2017). Spinal nociceptive circuit analysis with recombinant adeno-associated viruses: the impact of serotypes and promoters. *Journal of Neurochemistry*, *142*, 721–733.

Harrison, M., O'Brien, A., Adams, L., Cowin, G., Ruitenberg, M. J., Sengul, G., & Watson, C. (2013). Vertebral landmarks for the identification of spinal cord segments in the mouse. *NeuroImage*, *68*, 22–29.

Ishii, K., Nakamura, M., Dai, H., Finn, T. P., Okano, H., Toyama, Y., & Bregman, B. S. (2006). Neutralization of ciliary neurotrophic factor reduces astrocyte production from transplanted neural stem cells and promotes regeneration of corticospinal tract fibers in spinal cord injury. *Journal of Neuroscience Research*, *84*, 1669–1681.

Ito, S., Nagoshi, N., Kamata, Y., Kojima, K., Nori, S., Matsumoto, M., Takei, K., Nakamura, M., & Okano, H. (2021). LOTUS overexpression via ex vivo gene transduction further promotes recovery of motor function following human iPSC-NS/PC transplantation for contusive spinal cord injury. *Stem Cell Reports*, *16*, 2703–2717.

Ito, S., Nagoshi, N., Tsuji, O., Shibata S., Shinozaki M., Kawabata S., Kojima K., Yasutake K., Hirokawa T., Matsumoto M., Takei K., Nakamura M., Okano H. (2018) LOTUS inhibits neuronal apoptosis and promotes tract regeneration in contusive spinal cord injury model mice. *eNeuro 5*(5), 1–16.

Iwanami, A., Kaneko, S., Nakamura, M., Kanemura, Y., Mori, H., Kobayashi, S., Yamasaki, M., Momoshima, S., Ishii, H., Ando, K., Tanioka, Y., Tamaoki, N., Nomura, T., Toyama, Y., & Okano, H. (2005). Transplantation of human neural stem cells for spinal cord injury in primates. *Journal of Neuroscience Research*, *80*, 182–190.

Kadoya, K., Lu, P., Nguyen, K., Lee-Kubli, C., Kumamaru, H., Yao, L., Knackert, J., Poplawski, G., Dulin, J. N., Strobl, H., Takashima, Y., Biane, J., Conner, J., Zhang, S. C., & Tuszynski, M. H. (2016). Spinal cord reconstitution with homologous neural grafts enables robust corticospinal regeneration. *Nature Medicine*, *22*, 479–487.

Kajikawa, K., Imaizumi, K., Shinozaki, M., Shibata, S., Shindo, T., Kitagawa, T., Shibata, R., Kamata, Y., Kojima, K., Nagoshi, N., Matsumoto, M., Nakamura, M., & Okano, H. (2020). Cell therapy for spinal cord injury by using human iPSC-derived region-specific neural progenitor cells. *Molecular Brain*, *13*, 120.

Kamiyama, T., Kameda, H., Murabe, N., Fukuda, S., Yoshioka, N., Mizukami, H., Ozawa, K., & Sakurai, M. (2015). Corticospinal tract development and spinal cord innervation differ between cervical and lumbar targets. *The Journal of Neuroscience*, *35*, 1181–1191.

Kawai, M., Imaizumi, K., Ishikawa, M., Shibata, S., Shinozaki, M., Shibata, T., Hashimoto, S., Kitagawa, T., Ago, K., Kajikawa, K., Shibata, R., Kamata, Y., Ushiba, J., Koga, K., Furue, H., Matsumoto, M., Nakamura, M., Nagoshi, N., & Okano, H. (2021). Long-term selective stimulation of transplanted neural stem/progenitor cells for spinal cord injury improves locomotor function. *Cell Reports*, *37*, 110019.

Kinoshita, M., Matsui, R., Kato, S., Hasegawa, T., Kasahara, H., Isa, K., Watakabe, A., Yamamori, T., Nishimura, Y., Alstermark, B., Watanabe, D., Kobayashi, K., & Isa, T. (2012). Genetic dissection of the circuit for hand dexterity in primates. *Nature*, *487*, 235–238.

Kita, T., & Kita, H. (2012). The subthalamic nucleus is one of multiple innervation sites for long-range corticofugal axons: a single-axon tracing study in the rat. *The Journal of Neuroscience*, *32*, 5990–5999.

Kitagawa, T., Nagoshi, N., Kamata, Y., Kawai, M., Ago, K., Kajikawa, K., Shibata, R., Sato, Y., Imaizumi, K., Shindo, T., Shinozaki, M., Kohyama, J., Shibata, S., Matsumoto, M., Nakamura, M., & Okano, H. (2022). Modulation by DREADD reveals the therapeutic effect of human iPSC-derived neuronal activity on functional recovery after spinal cord injury. *Stem Cell Reports*, *17*, 127–142.

Kojima, K., Miyoshi, H., Nagoshi, N., Kohyama, J., Itakura, G., Kawabata, S., Ozaki, M., Iida, T., Sugai, K., Ito, S., Fukuzawa, R., Yasutake, K., Renault-Mihara, F., Shibata, S., Matsumoto, M., Nakamura, M., &

Okano, H. (2019). Selective ablation of tumorigenic cells following human induced pluripotent stem cell-derived neural stem/progenitor cell transplantation in spinal cord injury. *Stem Cells Translational Medicine*, *8*, 260–270.

Kondo, T., Saito, R., Otaka, M., Yoshino-Saito K., Yamanaka A., Yamamori T., Watakabe A., Mizukami H., Schnitzer M. J., Tanaka K. F., Ushiba J., Okano H. (2018) Calcium transient dynamics of neural ensembles in the primary motor cortex of naturally behaving monkeys. *Cell Reports 24*, 2191–2195 e2194, 2191, 2195.e4.

Kumamaru, H., Lu, P., Rosenzweig, E. S., Kadoya, K. and Tuszynski, M. H. (2019) Regenerating corticospinal axons innervate phenotypically appropriate neurons within neural stem cell grafts. *Cell Reports 26*, 2329–2339 e2324, 2329, 2339.e4.

Lemon, R. N. (2008). Descending pathways in motor control. *Annual Review of Neuroscience*, *31*, 195–218.

Liang, H., Paxinos, G., & Watson, C. (2011). Projections from the brain to the spinal cord in the mouse. *Brain Structure & Function*, *215*, 159–186.

Liang, H., Paxinos, G., & Watson, C. (2012). The red nucleus and the rubrospinal projection in the mouse. *Brain Structure & Function*, *217*, 221–232.

Liu, Y., Latremoliere, A., Li, X., Zhang, Z., Chen, M., Wang, X., Fang, C., Zhu, J., Alexandre, C., Gao, Z., Chen, B., Ding, X., Zhou, J. Y., Zhang, Y., Chen, C., Wang, K. H., Woolf, C. J., & He, Z. (2018). Touch and tactile neuropathic pain sensitivity are set by corticospinal projections. *Nature*, *561*, 547–550.

Liu, Y., Wang, X., Li, W., Zhang, Q., Li, Y., Zhang, Z., Zhu, J., Chen, B., Williams, P. R., Zhang, Y., Yu, B., Gu, X., & He, Z. (2017). A sensitized IGF1 treatment restores corticospinal axon-dependent functions. *Neuron*, *95*, 817-833.

Lu, T., Peng, W., Liang, Y., Li, M., Li, D. S., Du, K. H., Zhu, J. H., & Wu, J. H. (2020). PTEN-silencing combined with ChABC-overexpression in adipose-derived stem cells promotes functional recovery of spinal cord injury in rats. *Biochemical and Biophysical Research Communications*, *532*, 420–426.

Matsuzaki, Y., Konno, A., Mukai, R., Honda, F., Hirato, M., Yoshimoto, Y., & Hirai, H. (2017). Transduction profile of the marmoset central nervous system using adeno-associated virus serotype 9 vectors. *Molecular Neurobiology*, *54*, 1745–1758.

Moreno-Lopez, Y., Bichara, C., Delbecq, G., Isope, P., & Cordero-Erausquin, M. (2021). The corticospinal tract primarily modulates sensory inputs in the mouse lumbar cord. *eLife*, *10*, 1–19.

Network, B. I. C. C. (2021). A multimodal cell census and atlas of the mammalian primary motor cortex. *Nature*, *598*, 86–102.

Nori, S., Okada, Y., Yasuda, A., Tsuji, O., Takahashi, Y., Kobayashi, Y., Fujiyoshi, K., Koike, M., Uchiyama, Y., Ikeda, E., Toyama, Y., Yamanaka, S., Nakamura, M., & Okano, H. (2011). Grafted human-induced pluripotent stem-cell-derived neurospheres promote motor functional recovery after spinal cord injury in mice. *Proceedings of the National Academy of Sciences of the United States of America*, *108*, 16825–16830.

Okubo, T., Iwanami, A., Kohyama, J., Itakura, G., Kawabata, S., Nishiyama, Y., Sugai, K., Ozaki, M., Iida, T., Matsubayashi, K., Matsumoto, M., Nakamura, M., & Okano, H. (2016). Pretreatment with a gamma-secretase inhibitor prevents tumor-like overgrowth in human iPSC-derived transplants for spinal cord injury. *Stem Cell Reports*, *7*, 649–663.

Okubo, T., Nagoshi, N., Kohyama, J., Tsuji, O., Shinozaki, M., Shibata, S., Kase, Y., Matsumoto, M., Nakamura, M., & Okano, H. (2018). Treatment with a gamma-secretase inhibitor promotes functional recovery in human iPSC- derived transplants for chronic spinal cord injury. *Stem Cell Reports*, *11*, 1416–1432.

Oswald, M. J., Tantirigama, M. L., Sonntag, I., Hughes, S. M., & Empson, R. M. (2013). Diversity of layer 5 projection neurons in the mouse motor cortex. *Frontiers in Cellular Neuroscience*, *7*, 174.

Peters, A. J., Lee, J., Hedrick, N. G., O'Neil, K., & Komiyama, T. (2017). Reorganization of corticospinal output during motor learning. *Nature Neuroscience*, *20*, 1133–1141.

Peterson, B. W., Maunz, R. A., Pitts, N. G., & Mackel, R. G. (1975). Patterns of projection and braching of reticulospinal neurons. *Experimental Brain Research*, *23*, 333–351.

Roostalu, U., Salinas, C. B. G., Thorbek, D. D., Skytte, J. L., Fabricius, K., Barkholt, P., John, L. M., Jurtz, V. I., Knudsen, L. B., Jelsing, J., Vrang, N., Hansen, H. H., & Hecksher-Sørensen, J. (2019). Quantitative whole-brain 3D imaging of tyrosine hydroxylase-labeled neuron architecture in the mouse MPTP model of Parkinson's disease. *Disease Models & Mechanisms*, *12*, dmm04200.

Ropper, A. E., Thakor, D. K., Han, I., Yu, D., Zeng, X., Anderson, J. E., Aljuboori, Z., Kim, S. W., Wang, H., Sidman, R. L., Zafonte, R. D., & Teng, Y. D. (2017). Defining recovery neurobiology of injured spinal cord by synthetic matrix-assisted hMSC implantation. *Proceedings of the National Academy of Sciences of the United States of America*, *114*, E820–E829.

Sahni, V., Shnider, S. J., Jabaudon, D., Song, J. H. T., Itoh, Y., Greig, L. C., & Macklis, J. D. (2021). Corticospinal neuron subpopulation-specific developmental genes prospectively indicate mature segmentally specific axon projection targeting. *Cell Reports*, *37*, 109843.

Schmid, B., Tripal, P., Fraaß, T., Kersten, C., Ruder, B., Grüneboom, A., Huisken, J., & Palmisano, R. (2019). 3Dscript: animating 3D/4D microscopy data using a natural-language-based syntax. *Nature Methods*, *16*, 278–280.

Sheikh, I. S., Keefe, K. M., Sterling, N. A., Junker, I. P., Eneanya, C. I., Liu, Y., Tang, X. Q., & Smith, G. M. (2018). Retrogradely transportable lentivirus tracers for mapping spinal cord locomotor circuits. *Frontiers in Neural Circuits*, *12*, 60.

Shinozaki, M., Nagoshi, N., Nakamura, M., & Okano, H. (2021). Mechanisms of stem cell therapy in spinal cord injuries. *Cells*, *10*, 2676.

Slingsby, L. S., & Waterman-Pearson, A. E. (2000). The post-operative analgesic effects of ketamine after canine ovariohysterectomy—a comparison between pre- or post-operative administration. *Research in Veterinary Science*, *69*, 147–152.

Soderblom, C., Lee, D. H., Dawood, A., Carballosa M., Santamaria A. J., Benavides F. D., Jergova S., Grumbles R. M., Thomas C. K., Park K. K., Guest J. D., Lemmon V. P., Lee J. K., Tsoulfas P. (2015) 3D Imaging of axons in transparent spinal cords from rodents and non-human primates. *eNeuro 2*(2), 1–24.

Steward, O., Yee, K. M., Metcalfe, M., Willenberg, R., Luo, J., Azevedo, R., Martin-Thompson, J. H., & Gandhi, S. P. (2021). Rostro-caudal specificity of corticospinal tract projections in mice. *Cerebral Cortex*, *31*, 2322–2344.

Sun, L., Tang, Y., Yan, K., Yu, J., Zou, Y., Xu, W., Xiao, K., Zhang, Z., Li, W., Wu, B., Hu, Z., Chen, K., Fu, Z. F., Dai, J., & Cao, G. (2019). Differences in neurotropism and neurotoxicity among retrograde viral tracers. *Molecular Neurodegeneration*, *14*, 8.

Tennant, K. A., Adkins, D. L., Donlan, N. A., Asay, A. L., Thomas, N., Kleim, J. A., & Jones, T. A. (2011). The organization of the forelimb representation of the C57BL/6 mouse motor cortex as defined by intracortical microstimulation and cytoarchitecture. *Cerebral Cortex (New York, N.Y: 1991)*, *21*, 865–876.

Tervo, D. G., Hwang, B. Y., Viswanathan, S., Gai, T., Lavzin, M., Ritola, K. D., Lindo, S., Michael, S., Kuleshova, E., Ojala, D., Huang, C., Gerfen, C. R., Schiller, J., Dudman, J. T., Hantman, A. W., Looger, L. L., Schaffer, D. V., & Karpova, A. Y. (2016). A designer AAV variant permits efficient retrograde access to projection neurons. *Neuron*, *92*, 372–382.

Tsuji, O., Miura, K., Okada, Y., Fujiyoshi, K., Mukaino, M., Nagoshi, N., Kitamura, K., Kumagai, G., Nishino, M., Tomisato, S., Higashi, H., Nagai, T., Katoh, H., Kohda, K., Matsuzaki, Y., Yuzaki, M., Ikeda, E., Toyama, Y., Nakamura, M., … Okano, H. (2010). Therapeutic potential of appropriately evaluated safe-induced pluripotent stem cells for spinal cord injury. *Proceedings of the National Academy of Sciences of the United States of America*, *107*, 12704–12709.

Ueno, M., Nakamura, Y., Li, J., Gu Z., Niehaus J., Maezawa M., Crone S. A., Goulding M., Baccei M. L., Yoshida Y. (2018) Corticospinal circuits from the sensory and motor cortices differentially regulate skilled movements through distinct spinal interneurons. *Cell Reports 23*, 1286–1300 e1287, 1286, 1300.e7.

Wagner, A. E., Walton, J. A., Hellyer, P. W., Gaynor, J. S., & Mama, K. R. (2002). Use of low doses of ketamine administered by constant rate infusion as an adjunct for postoperative analgesia in dogs. *Journal of the American Veterinary Medical Association*, *221*, 72–75.

Wang, X., Liu, Y., Li, X., Zhang Z., Yang H., Zhang Y., Williams P. R., Alwahab N. S.A., Kapur K., Yu B., Zhang Y., Chen M., Ding H., Gerfen C. R., Wang K. H., He Z. (2017) Deconstruction of Corticospinal Circuits for Goal-Directed Motor Skills. *Cell 171*, 440–455 e414, 440, 455. e14.

Wang, Z., Maunze, B., Wang, Y., Tsoulfas, P., & Blackmore, M. G. (2018). Global Connectivity and Function of Descending Spinal Input Revealed by 3D Microscopy and Retrograde Transduction. *The Journal of Neuroscience*, *38*, 10566–10581.

Williams, P. T., & Martin, J. H. (2015). Motor cortex activity organizes the developing rubrospinal system. *The Journal of Neuroscience*, *35*, 13363–13374.

SUPPORTING INFORMATION

Additional supporting information can be found online in the Supporting Information section at the end of this article.

How to cite this article: Lu, T., Shinozaki, M., Nagoshi, N., Nakamura, M., & Okano, H. (2022). 3D imaging of supraspinal inputs to the thoracic and lumbar spinal cord mapped by retrograde tracing and light-sheet microscopy. *Journal of Neurochemistry*, *162*, 352–370. https://doi.org/10.1111/jnc.15653